

https://dspace.org/

Gamma ray fluorescence for in situ evaluation of ore in Witwatersrand gold mines

Rolle, Rainer

2015-08-18
http://hdl.handle.net/10539/18258

Downloaded from a DSpace repository. https://dspace.org/

Experimentally it was found that the most prominent gold peak in the normalized Co-57 spectrum i.e. the Au $K\alpha_1$ peak, had a net peak height slightly lower than the Au $K\beta_1'$ peak in the comparable Cd-109 spectrum. The peak-to-background ratio for the same gold concentration was more than three times higher in the latter spectrum i.e. $R_{Cd} \Rightarrow 3R_{Co}$. From equation 7.4 for similar peak heights, therefore, Co-57 requires a measuring period more than three times longer than that for Cd-109, to attain the same coefficient-of-variation of the peak-to-background ratio at the same gold concentration.

Although in the Te-123m spectrum the Au $K\alpha_1$ peak had about 1,3 times the intensity of the $K\beta_1'$ peak in the Cd-109 spectrum, the background under the $K\alpha_1$ peak was 2,2 times higher than that under the $K\beta_1'$. Equation 7.4 shows a 2,2 times longer measuring period for Te-123m if the peaks had been equal, but the increased intensity of the $K\alpha$ peak requires that equation 7.3 be used, so that the actual measuring period is $2,2/(1,3)^2 = 1,3$ times longer than that for Cd-109.

For in situ gold ore valuation, where rapid measurement is required, the much shorter measuring time using Cd-109 easily compensates for its higher cost relative to Co-57 and Te-123m.

7.3 Measurement of the Cd-109 gold ore spectrum

The optimum scheme for evaluating the spectrum characterized by the relevant spectral region has two gold $K\beta'$ peaks on a nearly exponentially decreasing background needs to be determined. Lead $K\alpha_1$ and $K\beta_1'$ peaks are situated on either

side of the Au Kβ′ peaks. The only other elements whose Kβ lines lie closer to the Au Kβ lines than the Pb Kβ lines, namely Ir, Pt, Hg, and Tl do not occur in significant quantities in the Witwatersrand gold deposits. Interfering Kα peaks for elements heavier than lead cannot occur in this region because the K lines of such elements are not excited by the 88 keV photons of Cd-109.

Although a positive correlation between gold and uranium, and its associated natural radioactivity and lead, is known to exist in the deposits, the correlation often is poor and cannot be relied upon. The lead peaks must, therefore, be considered as an uncorrelated interference that limits the spectral region available for the evaluation of the background under the gold Kβ′ peaks.

Similarly in the measurement of rough samples where the measuring geometry may vary widely the background beyond the lead K lines is not well enough correlated with the background under the gold peaks and cannot, therefore, be used in the evaluation of the gold region.

The 70 to 90 keV region of the fluorescence spectrum of pure gold and lead is shown in Figure 7.2. The energies and relative intensities of the K lines are listed in Table 7.1 (Lederer, 1967).

Measured relative intensities from thick samples differ a few percent from the listed values because of matrix absorption.

In preliminary measurements, a pseudo-two-channel scheme was employed for the evaluation of the Au $K\beta'_1$ peak only. One window was placed arbitrarily over the peak while two

background windows which were counted in the same register, were placed between the Pb $K\alpha_1$ and Au $K\beta_1'$ peaks and between the Au $K\beta_1'$ and Au $K\beta_2'$ peaks. System energy resolution gave some concern as it was thought necessary for the Au $K\beta_1'$ and the Au $K\beta_2'$ peaks to be well enough resolved to allow an adequate "clear background" window between them.

The Au $K\beta_1'$ peak was certainly the most prominent peak and the listed K line intensities and observed background intensities seemed to indicate that it would hardly be worthwhile to include the Au $K\beta_2'$ peak in the evaluation. When it came to optimising the six discriminator positions, however, closer investigation showed that, when background intensity per mean peak width is considered, the peak to background intensity ratios for the Au $K\beta_1'$ and $K\beta_2'$ peaks are about the same. It was found that since the $K\beta_2'/K\beta_1'$ peak intensities had a ratio which was approximately 9/35, measurement times would have been increased by about 9/35 i.e. 25%, by not including the $K\beta_2'$ peak. Since inclusion of the $K\beta_2'$peak would involve little or no added instrumental complexity, this change was considered worthwhile.

Detailed analysis of the two peak measurement will be deferred (chapter 9) so that it may be combined with the optimisation of signal processing parameters.

8 FUNDAMENTALS IN RANDOM SIGNAL PROCESSING

In routine application where as much rock as possible should be sampled in a given time and valued to a given precision, it is important that all parts of the valuation system should be optimised as a whole. Data acquisition for trace elements is an inherently slow process, and the processing of detector signals thus must be efficient and of high quality to reduce the time for data acquisition to a minimum. In most discussions on random signal processing times only the fundamentals of the basic processes are dealt with. In this chapter comprehensive equations, including new concepts of pileup overlap parameters, developed from first principles, are presented. These permit optimisation of the signal processing system as a whole.

The efficiency of signal processing can be expressed as the usable output count-rate divided by the detected event rate for any one spectral component; it is synonymous with the probability P that an event will be analysed without pileup distortion, and with the true livetime fraction. In what follows, P* with the asterisk will indicate the probability that a randomly detected event is processed inclusive of pileup distortion. In a complementary way percentage deadtime is a measure of inefficiency. Energy resolution and freedom from spectral distortion are measures of system quality rather than efficiency.

8.1 Extending and non-extending processing times

Every detected photon gives rise to a signal sequence which must be above the noise threshold for the finite time required to process the signal. In the processing of signals from randomly occurring events, there are two types of processes, extending and non-extending. Extending processes, variously known as self-prolonging, paralysable or retriggerable, occur for every event irrespective of other events, e.g. the amplifier pulse width w^* in solid state detector systems. Non-extending processes occur if signals that have met certain conditions are processed a particular way, e.g. analog-to-digital conversion of duration t^* in pulse height analysis.

When simply counting above the noise level is required, the probability that a randomly detected event gives rise to an extending pulse is given by the familiar expression

$$P^* = 1/\mathrm{Exp}(rw^*) \qquad 8.1$$

where r = total detected event rate

and w^* = pulse width for a single event.

For purely non-extending processes of duration t^* the expression would be:-

$$P^* = 1/(1+rt^*) \xrightarrow[0]{rt^*} 1/\mathrm{Exp}(rt^*) \qquad 8.2$$

When both types of processes occur for the same event they do not usually commence simultaneously, e.g. in energy analysis the optimum point for analysing the height of a pulse occurs a time ℓ^* after the event, ℓ^* usually being the leading edge of a pulse or the time-to-peak, for a pulse from a single event. It is at this point where non-extending processes of duration t^* usually start; part or all of t^*

may run concurrently with the trailing edge $w^*-\ell^*$ of the amplifier pulse, i.e. with part or all of the extending processing time. These parameters are illustrated in Figure 8.1.

The leading edge of a pulse normally is shorter than the trailing edge i.e. $\ell^* <= w^*/2$. The opposite situation, however, would not alter the processing efficiency.

8.2 Processing overlap parameters

The random occurrence of detected events inevitably leads to the overlap of the processing times of different events.

If any two events follow each other very closely, and if this can be detected, then one or both events may be rejected from final signal processing which could in this

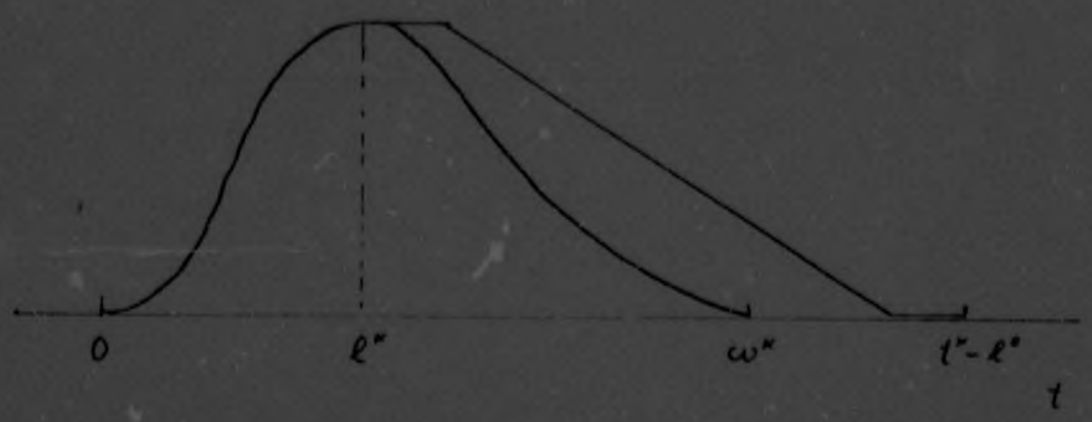


FIGURE 8.1 ANALOG PULSE PROCESSING TIMES

case possibly be perturbed. Such rejection would thus reduce spectral distortion. Whether or not a specific event will undergo final processing depends on timing conditions which can be defined by three overlap parameters , namely p , α and β as follows:

- p - In any processing systems there is always a lower time limit p within which two or more randomly occurring events cannot be recognised separately and will be processed as a single pulse. The parameter p is normally referred to as the pulse-pair-resolution time for pileup rejection. In energy analysis, if p is small relative to w* and the height of the amplifier pulse is nearly constant over a time p near its peak, then practically full summing of analysed pileup events will result from peak-on-peak pileup. Larger values of p will also allow analysis of leading edge and trailing edge pileup pulses. This overlap parameter always has a finite value that cannot exceed w*, i.e. $0<=p<=w^*$,

- α - If the time between a current event and the next event is greater than $\ell^* + \alpha$ then the current event will not be rejected by the next event; in pulse height analysis if $-\ell^* <= \alpha < 0$ then spectral distortion will be caused by amplifier leading pileup - hence α will be referred to as the leading overlap limit, and

- β - If the time between the end of the processing time of a previous event and a current event is greater than $\beta - \ell^*$ then the current event will not be rejected by the previous one; if $-(w^* - \ell^*) <= \beta < 0$ then spectral distortion will be caused by trailing edge pileup - thus β will be

referred to as the trailing overlap limit.

Negative leading and trailing overlap limits are mutually exclusive with p so that $-w^* <= \alpha + \beta - p$. Positive values cause unnecessary rejection but do not cause pileup distortion of the spectrum.

The introduction of these overlap parameters greatly simplifies the derivation of the signal processing efficiency P.

8.3 Effective processing time and efficiency

The probability P that a randomly detected event will be processed without pileup distortion can still be expressed simply with the following effective parameters

$w = w^* + \alpha + \beta + p$ = effective extending processing time

$\ell = \ell^* + \alpha$ = effective leading edge 8.3

and $t = t^* + \beta + p$ = effective non-ext. processing time

For extending processes

$$P = 1/Exp(rw) \qquad 8.4$$

and for purely non-extending processes

$$P = 1/(1 + rt) \qquad 8.5$$

The absence of the asterisk indicates that effective parameters are used and that the probability excludes the pileup distorted part of the processed spectrum. P is a more realistic measure of system efficiency than P* particularly in signal processing not followed by data processing that unfolds pileup spectra.

When both extending and non-extending processes occur the probability becomes (see Appendix 8.6) -

$$P = 1/[e^{rw} + e^{r\ell}(1-e^{-rt'}) + rt''] \qquad 8.6$$

where t′ and t″ depend on how much the non-extending process

lengthens the extending process as given in Table 8.1.

Equations 8.4 and 8.5 are readily seen to be the limiting conditions of equation 8.6. If the total detected event rate r consists of spectral components r_n (i.e. $r = \sum^{n} r_n$) where the subscript n refers to events of energy between n and n + 1, and if the effective non-extending processing time t varies as t_n, as for example in ramp type analog to digital conversion systems, then the probability, this time in original parameters, becomes

$$P = 1/[e^{r(w^*+\alpha+\beta+p)} + e^{r(\ell^*+\alpha)}(1-\sum^{n} e^{-rt'_n r_n/r}) + \sum^{n} r_n t''_n] \quad 8.7$$

the summations extending over all detected components.

Table 8.1 Effective non-extending processing times

Process relationship	t'	t''
$t_n <= w - \ell$	0	0
($t_n^* <= w^* - \ell^*$	0	0)
$w - \ell < t_n <= w$	$t_n - w + \ell$	0
($w^* - \ell^* < t_n^* <= w^* + \alpha$	$t_n^* - w^* + \ell^*$	0)
$w < t_n$	ℓ	$t_n - w$
($w^* + \alpha < t_n^*$	$\ell^* + \alpha$	$t_n^* - w^* - \alpha$)

The foregoing equations have wide applicability in random event processing systems. They can be used from the simplest counting systems to high-rate coincidence spectrometry and pulsed-optical feedback detection systems to provide a precise measure of the efficiency of data acquisition. Their analytical nature forms a basis for evaluating systematic errors in a wide variety of timing

systems used in present-day random-event processors.

8.4 Relative importance of various processing parameters

In most pulse processing systems, only the familiar parameters w* and ℓ* are specified.

The extending parameters w* and ℓ* are usually expressed in time constants TC, w* ranging down to 5,5TC or even lower, and ℓ* usually around 2,2TC for modern semi-Gaussian amplifiers.

For high-energy (MeV) analysis with solid-state detectors of about 0,1% resolution at full-width half maximum (FWHM) the optimum TC at low count rates is about 2 μs (i.e. w*≈10 μs) while for low energy (keV) analysis with detectors of ≈3% FWHM resolution, time constants up to 10 μs (i.e. w*≈50 μs) are often recommended by the manufacturers.

The non-extending time t* in ramp-type pulse-height-convertors of 100 MHz rundown frequency ranges from around 50 μs at 0,1% FWHM resolution to about 5 μs at 10% FWHM resolution.

Table 8.1 shows that only the portion of the non-extending processing time that is not already taken up by extending processing time reduces the processing efficiency P. At low energies where t* is usually less than w*-ℓ*, the non-extending time t* hardly influences P; although at high energies P can be reduced substantially more by t* than by w* if ℓ* is greater than w*-ℓ* for most of the detected spectral components. However, if only one or two minor spectral components are of interest then, as equation 8.6 shows, the extending processing time can become the dominant one even at high energies. For the analysis of

a single element at trace concentrations, the signal processing efficiency with ramp-type pulse-height-converters can thus be practically the same as with discrete pulse-height-discriminators having much smaller t*.

In most commercial spectrometry systems the combined overlap times $\alpha + \beta + p$ can readily amount to $w^*/2$ and influence P by an additional half as much as w^*.

Whereas negative values of α and β result in pileup distortion of the spectral background and positive values of α and β cause unnecessary rejection of good amplifier pulses, zero values allow the highest signal processing efficiency with the lowest pileup distortion.

In systems without specific pileup rejection, trailing-edge pileup distortion can be overcome simply by analysing only the first peak in a pulse starting from the noise threshold. In these systems $\beta \Rightarrow \ell^*$, an excessive positive value, and because $\alpha = -p = -\ell^*$ leading-edge pileup distortion occurs.

In systems with specific pileup rejection p is considerably smaller than ℓ^* and $\alpha \Rightarrow 0$. However, almost always it is found that $\beta \Rightarrow \ell^*$ whereas practically zero values could readily be implemented for both α and β.

Commercially available systems are thus seen to be somewhat wasteful in rejecting amplifier pulses unnecessarily. At low count rates, i.e. for $rw < 0{,}1$, where most systems tend to be operated, this hardly matters, but at increasingly higher rates this aspect becomes progressively more important.

For a given effective extending processing time w, the

spectrum acquisition rate for any component $r_n P$ reaches a maximum at a total detected rate $r = 1/w$. At higher rates the signal processing is very inefficient i.e. $P = 1/e = 0{,}368$, and well before the efficiency has dropped this low it may be advisable to trim w^*. Reductions in w^* must, however, be carried out judiciously as they worsen the system energy resolution; a compromise between efficiency P and FWHM energy resolution is called for.

8. Pileup rejection

The need to reject amplifier pulse pileup is not always clearly understood. In systems where non-extending processing times t_n^* exceed the trailing edge $w^* - \ell^*$, non-rejected pileup pulses unnecessarily add to the total non-extending processing time, but in most cases the reduction in P is not significant. When for all spectral components $t_n^* <= w^* - \ell^*$, pileup rejection has no effect on the signal processing efficiency whatsoever.

Without rejection, pileup causes a count-rate-dependent background of relatively low intensity over the whole spectrum. For most spectral components where this pileup background slightly augments an intense natural background, pileup hardly affects the spectral quality. The real need for pileup rejection, however, arises for minor and trace spectral components that lie in a natural background region of low intensity which might be overshadowed by pileup background.

The total pileup intensity in spectrum acquisition, relative to the total natural spectrum intensity is given by $(e^{-r(\alpha+\beta-p)} - 1)$ where positive values of α and β are taken

as zero, because with positive values there is no pileup distortion. The pileup components of a spectrum are made up of (partial) energy summations of the natural spectral components. The relative spectral distortion in a particular spectral region of low intensity can thus be far more severe than the mean value for the total spectrum indicated by the above expression.

To sum up, the signal processing efficiency P of a system can be completely described in terms of the total detected event rate r, the familiar parameters w^*, ℓ^*, and t_n^* and the three overlap parameters p, α and β. The pulse width w^* or, more correctly, the system time constant TC influences the energy resolution, while the overlap parameters determine the degree of spectral distortion from pulse pileup.

8.6 Appendix: Derivation of equations

Mean of the number (1 + c) of events occurring for each analysed event.

In a PHA system every detected event is followed by an extending processing time:

w^* = amplifier pulse width

The point of optimum resolution for analysing the pulse height occurs at

ℓ^* = leading edge (time to peak)

after the event.

Only analysed events cause non-extending processing time

$t_n^* = n/f + mc$

where

n = channel number

f = ADC rundown frequency

mc = ADC stretcher + resetting time + memory storage cycle time

If p is the pulse pair resolution time for pileup rejection and if the pulse peak of an event has to occur at least an interval β after the end of the processing time of the previous event, and at least an interval α before the next event, in order not to be rejected, then:

$w = w^* + \alpha + \beta + p$ = effective extending processing time

$\ell = \ell^* + \alpha$ = effective leading edge

and $t_n = t_n^* + \beta + p$ = effective non-ext. processing time

When $-w^* <= \beta < 0$, spectral distortion is caused due to trailing edge pile-up and when $-\ell^* <= \alpha < 0$, spectral distortion is caused due to leading edge pile-up. Values of α and β equal to zero are the optimum for pile-up rejection, whereas positive values cause unnecessary rejection.

The non-extending processing time of non piled-up events starts at a time ℓ or ℓ^*, whichever is the larger, after the event. The trailing edge of the amplifier pulse overlaps with t_n^*.

The following equations are derived for $\ell^* <= \frac{1}{2}w$; symmetrical results would be obtained for $\ell^* => \frac{1}{2}w$.

Let

$$t = \begin{cases} w - \ell & \text{for } t_n <= w - \ell \\ t_n & \text{for } w - \ell < t_n <= w \\ w & \text{for } w < t_n \end{cases}$$

r = random event rate

Q(i) = probability that there will be i events between any two successive analysed events

A) Then for a fixed non-extending processing time $t_n <= w$ the Q(i)'s can be derived as:

$$Q(0) = e^{-rt}$$

$$Q(1) = (1-e^{-r(t-\ell)})e^{-rw}$$

$$Q(2) = (1-e^{-r(w-\ell)})(1-e^{-r(t-\ell)})e^{-rw} + (1-e^{-r\ell})e^{-r(w-\ell)}e^{-rt}$$

Let $W = (1 - e^{-r(w-\ell)})$

and $L = (1 - e^{-r\ell})e^{-r(w-\ell)}$

then

$$Q(2) = W\,Q(1) + LQ(0)$$

$$Q(3) = W^2Q(1) + W\,LQ(0) + LQ(1)$$

$$Q(4) = W^3Q(1) + W^2LQ(0) + 2W\,LQ(1) + L^2Q(0)$$

$$Q(5) = W^4Q(1) + W^3LQ(0) + 3W^2LQ(1) + 2WL^2Q(0) + L^2Q(1)$$

etc.

For i and j > 0 the jth term of Q(i) is

$$Q(i,j) = \begin{cases} \dfrac{(i - \frac{1}{2}j - \frac{1}{2})!}{(i-j)!\,(\frac{1}{2}j-\frac{1}{2})!}\, W^{i-j}L^{\frac{1}{2}j-\frac{1}{2}}Q(1) & \text{for odd } j \\ \dfrac{(i - \frac{1}{2}j - 1)!}{(i-j)!\,(\frac{1}{2}j-1)!}\, W^{i-j}\,L^{\frac{1}{2}j}\,Q(0) & \text{for even } j \end{cases}$$

Substituting

$$k = \begin{cases} \frac{1}{2}j + \frac{1}{2} & \text{for odd } j \\ \frac{1}{2}j & \text{for even } j \end{cases}$$

and $m = i - j$

the zeroeth statistical moment becomes

$$\sum_{i=0}^{\infty} Q(i) = Q(0) + \sum_{i=1}^{\infty}\sum_{j=1}^{i} Q(i,j)$$

$$= Q(0) + \sum_{k=1}^{\infty}[\{L^k\,Q(0) + L^{k-1}Q(1)\}\sum_{m=0}^{\infty}\frac{(k+m-1)!}{m!(k-1)!}W^m]$$

$$= Q(0) + \sum_{k=1}^{\infty}[\{L^kQ(0) + L^{k-1}Q(1)\}(1-W)^{-k}]$$

$$= Q(0) + (e^{rw}-1)Q(0) + e^{rw}Q(1)$$

$$= 1 = \text{the total probability}$$

and the first statistical moment becomes

$$\sum_{i=0}^{\infty} iQ(i) = \sum_{k=1}^{\infty}[\{L^k\,Q(0)\sum_{m=0}^{\infty}(m + 2k)\frac{(k+m-1)!}{m!(k-1)!}W^m\}$$

$$+ \{L^{k-1}Q(1)\sum_{m=0}^{\infty}(m+2k-1)\frac{(k+m-1)!}{m!(k-1)!}W^m\}]$$

$$= \sum_{k=1}^{\infty} \left[\left(\frac{L}{1-W}\right)^{k} Q(0) \frac{k(2-W)}{1-W} + \left(\frac{L}{1-W}\right)^{k-1} Q(1) \left(\frac{k}{(1-W)^2} + \frac{k-1}{1-W}\right) \right]$$

$$= \left\{Q(0)\frac{2-W}{1-W} + Q(1)\frac{1}{1-W}\right\}(1-e^{-r\ell})e^{2r\ell} + Q(1)\frac{1}{(1-W)^2} - e^{2r\ell}$$

$$= e^{rw} - 1 + e^{r\ell} - e^{r(w-t)}$$

$$= E[c] = E[1 + c] - 1$$

= the mean number of events between successive analysed events.

B) For a fixed non-extending processing time $t_n > w$ the events occurring during the trailing, non-extending interval $(t_n - w)$ are Poisson distributed with parameter $r(t_n - w)$. The above mean is thus increased by $r(t_n - w)$.

$$E[c] = e^{rw} - 1 + e^{r\ell} - e^{r(w-t)} + r(t_n - w)$$

C) For a variable non-extending processing time t_n where

r_n = rate of component n requiring a non-extending processing time t_n

Let

$$t' = t-w+ = \begin{cases} 0 \\ -t_n - w + \ell \\ \ell \end{cases} \quad \text{and} \quad t'' = \begin{cases} 0 & \text{for } t_n <= w-\ell \\ 0 & \text{for } w-\ell < t_n <= w \\ t_n - w & \text{for } w < t_n \end{cases}$$

then

$$E[1+c] = 1 + E[c]$$

$$= 1 + \sum^{p} (e^{rw} - 1 + e^{r\ell} - e^{r(\ell-t')} + rt'')r_n/r$$

$$= e^{rw} + e^{r\ell}(1 - \sum^{p} e^{-rt'} r_n/r) + \sum^{p} r_n t''$$

$$= 1/P \longrightarrow$$

which is the reciprocal probability that a detected event will be analysed without pileup distortion.

$$= \sum_{k=1}^{\infty} \left[\left(\frac{L}{1-W}\right)^{k} Q(0) \frac{k(2-W)}{1-W} + \left(\frac{L}{1-W}\right)^{k-1} Q(1) \left(\frac{k}{(1-W)^2} + \frac{k-1}{1-W}\right) \right]$$

$$= \left\{Q(0)\frac{2-W}{1-W} + Q(1)\frac{1}{1-W}\right\}(1-e^{-r\ell})e^{2r\ell} + Q(1)\frac{1}{(1-W)^2} - e^{2r\ell}$$

$$= e^{rw} - 1 + e^{r\ell} - e^{r(w-t)}$$

$$= E[c] = E[1 + c] - 1$$

= the mean number of events between successive analysed events.

B) For a fixed non-extending processing time $t_n > w$ the events occurring during the trailing, non-extending interval $(t_n - w)$ are Poisson distributed with parameter $r(t_n - w)$. The above mean is thus increased by $r(t_n - w)$.

$$E[c] = e^{rw} - 1 + e^{r\ell} - e^{r(w-t)} + r(t_n - w)$$

C) For a variable non-extending processing time t_n where

r_n = rate of component n requiring a non-extending processing time t_n

Let

$$t' = t-w+ = \begin{cases} 0 \\ -t_n - w + \ell \\ \ell \end{cases} \quad \text{and} \quad t'' = \begin{cases} 0 & \text{for } t_n \leq w-\ell \\ 0 & \text{for } w-\ell < t_n \leq w \\ t_n - w & \text{for } w < t_n \end{cases}$$

then

$$E[1+c] = 1 + E[c]$$

$$= 1 + \sum^{n} (e^{rw} - 1 + e^{r\ell} - e^{r(\ell-t')} + rt'')r_n/r$$

$$= e^{rw} + e^{r\ell}(1 - \sum^{n} e^{-rt'} r_n/r) + \sum^{n} r_n t''$$

$$= 1/P \longrightarrow$$

which is the reciprocal probability that a detected event will be analysed without pileup distortion.

9 ANALOG SIGNAL PROCESSING IN THE GOLD ANALYSER

9.1 The gold Kβ′ peaks

Quantitative evaluation of two intensity-correlated peaks would be straightforward if they were Gaussian. The $K\beta_1'$ and $K\beta_2'$ peaks are, however, an unresolved triplet and doublet respectively. Peak broadening can readily be observed in Figure 7.1 where only the Pb $K\alpha_1$ peak is a singlet. When the system had been adjusted for higher resolution, peak shoulders could be observed. For evaluation of peak-to-background ratios the individual lines need to be defined more precisely.

The $K\alpha_1$ and $K\alpha_2$ lines correspond to monoenergetic transitions from two L atomic levels to the K level. However, the energies listed in Table 7.1 for the β′ lines are averages of groups of transitions from three M atomic levels and two N levels. The Siegbahn notation for the individual lines and their energies, calculated from differences in binding energies (Lederer, 1967), is shown in Table 9.1.

A literature search for the relative individual intensities did not turn up reliable data. The values listed in ASTM DS46 (Johnson et al., 1970) do not total to the intensity means in Table 7.1 nor do they fit the observed peak shapes in Figure 7.1. It was, therefore, assumed that in the Siegbahn notation the lines had been numbered in

9 ANALOG SIGNAL PROCESSING IN THE GOLD ANALYSER

9.1 The gold Kβ′ peaks

Quantitative evaluation of two intensity-correlated peaks would be straightforward if they were Gaussian. The $K\beta_1'$ and $K\beta_2'$ peaks are, however, an unresolved triplet and doublet respectively. Peak broadening can readily be observed in Figure 7.1 where only the Pb $K\alpha_1$ peak is a singlet. When the system had been adjusted for higher resolution, peak shoulders could be observed. For evaluation of peak-to-background ratios the individual lines need to be defined more precisely.

The $K\alpha_1$ and $K\alpha_2$ lines correspond to monoenergetic transitions from two L atomic levels to the K level. However, the energies listed in Table 7.1 for the β′ lines are averages of groups of transitions from three M atomic levels and two N levels. The Siegbahn notation for the individual lines and their energies, calculated from differences in binding energies (Lederer, 1967), is shown in Table 9.1.

A literature search for the relative individual intensities did not turn up reliable data. The values listed in ASTM DS46 (Johnson et al., 1970) do not total to the intensity means in Table 7.1 nor do they fit the observed peak shapes in Figure 7.1. It was, therefore, assumed that in the Siegbahn notation the lines had been numbered in

Table 9.1 Individual K X-ray lines of gold and lead

LINE		LEVEL TRANSITION	ESTTD. INTENSITY	ENERGY (keV) Au	ΔE	Pb
$K\alpha_2$		L_{II} - K	55	66,99		72,80
$K\alpha_1$		L_{III} - K	(100)	68.81	2,61	74,97
$K\beta_1'$	$K\beta_3$	M_{II} - K	3 - 6	77,58	0,40	84,45
	$K\beta_1$	M_{III} - K	26 - 32	77,98	0,45	84,94
	$K\beta_5$	M_{IV} - K	0,5 - 3	78,43	1,65	85,42
$K\beta_2'$	$K\beta_4$	N_{II} - K	3 - 4,5	80,08	0,10	87,24
	$K\beta_2$	N_{III} - K	4,5 - 6	80,18	4,27	87,36

order of decreasing intensity as expected from calculated transition probabilities; estimated intensities based on this assumption are included in Table 9.1.

Instead of treating the five gold lines individually, the $K\beta_1'$ and $K\beta_2'$ peaks can be handled as approximately Gaussian peaks having effective peak resolutions wider than the Pb $K\alpha_1$ peak. Because the two gold peaks are correlated their ratios can be treated as one composite peak in calculating the peak-to-background ratio.

9.2 Maximum available background region

In deciding on the maximum available background region t_{max} in units of σ, available for the evaluation of the peak-to-background ratio, first the available energy region needs to be determined from the interfering Pb $K\alpha_1$ and $K\beta_3$ line energies and the system energy resolution Γ. Next the

effective energy resolution of the Au $K\beta_1$ and Au $K\beta_2$ peaks must be defined in terms of Γ. Compensation must be made for the change from a constant background to a sloping background. This is done by adjusting the t_{max}, determined from the energy resolution and separation of the gold and lead peaks, by the ratio of the background intensity under the gold peaks and the adjacent regions.

The FWHM system energy resolution was given in eq.5.1

$$\Gamma = \sqrt{[\ 5{,}5FcE\ +\ \Gamma_n^2\ ]} \qquad 9.1a$$

over the limited range between the Pb Kα and Kβ lines $\sqrt{E}$ is practically constant. Thus, taking an average energy of 80 keV, the system resolution is

$$\Gamma = \sqrt{(406^2\ +\ \Gamma_n^2\ )}\ eV \qquad 9.1b$$

which can be written linearly as the fundamental resolution plus a noise term:-

$$\Gamma = 406eV\ +\ {}^*\Gamma_n \qquad 9.1c$$

where ${}^*\Gamma_n$ is the equivalent quadrature summed noise contribution. For detector systems under consideration ${}^*\Gamma_n$ ranges from about 50eV to 400eV.

Interference from lead peaks depends on the intensity of the lead peak tails included in the background evaluation. If exceptionally strong lead peaks are not to bias the measurement of small gold peaks ($R \sim 0{,}1$) by more than 10% (negatively) then the background region employed should not come within 4 σ (i.e. 1,7 FWHM) of the Pb $K\alpha_1$ and Pb $K\beta_3$ lines. The total energy region available is thus -

Pb $K\alpha_1$		Pb $K\beta_3$		
from	$74970 + 1{,}7\ \Gamma$	to	$84450 - 1{,}7\ \Gamma$ eV	9.2a
i.e. from	$75650 + 1{,}7{}^*\Gamma_n$	to	$83770 - 1{,}7{}^*\Gamma_n$ eV	9.2b

Working with the blank backscatter spectrum in Figure 4.1 the intensity in this region relative to the total spectrum intensity was found to be

$$\frac{\Gamma_n}{\Gamma} = 7{,}36\times10^{-3} - 3{,}84\times10^{-6} * \Gamma_n \qquad 9.2c$$

The effective resolution of the Kβ′ peaks in this region is given by the system resolution Γ and broadening from the 400eV and 100eV separation of the dominant β lines. The broadening cannot exceed the separation at high resolution and tapers off at poorer resolution. Over the limited resolution range where Gaussian approximation of the multiplets is appropriate the effective resolution of the β′ peaks was measured over a range of time constants, changing Γ, and was determined as

$$\Gamma\ [\beta_1'] \quad 500 + 0{,}5\,\Gamma\ \text{eV} = 703 + 0{,}5 * \Gamma_n\ \text{eV} \qquad 9.3a$$

$$\text{and } \Gamma\ [\beta_2'] \quad 60 + \quad \Gamma\ \text{eV} = 463 + \quad * \Gamma_n\ \text{eV} \qquad 9.3b$$

The FWHM energy regions for the Au $K\beta_1'$ and Au $K\beta_2'$ peaks are based upon the data given in Table 9.1, thus:

$$77900 \pm \tfrac{1}{2}\Gamma[\beta_1'] \quad \text{i.e. from } 77540 - \tfrac{1}{2} * \Gamma_n \text{ to } 78251 + \tfrac{1}{2} * \Gamma_n \qquad 9.4a$$

$$\text{and } 80100 \pm \tfrac{1}{2}\Gamma[\beta_2'] \quad \text{i.e. from } 79868 - \tfrac{1}{2} * \Gamma_n \text{ to } 80332 + \tfrac{1}{2} * \Gamma_n \qquad 9.4b$$

The relative intensities of the background spectrum in Figure 4.1 for these regions were found to be

$$\frac{\Gamma_n}{\Gamma} = 8{,}24\times10^{-4} + 5{,}75\times10^{-7} * \Gamma_n \qquad 9.5a$$

$$\text{and } \frac{\Gamma_n}{\Gamma} = 3{,}03\times10^{-4} + 7{,}57\times10^{-7} * \quad _n \qquad 9.5b$$

respectively, giving a total FWHM $\beta_1' + \beta_2'$ relative background intensity

$$\frac{\Gamma_n}{\Gamma} = 1{,}13\times10^{-3} + 1{,}33\times10^{-6} * \Gamma_n \qquad 9.5c$$

The total available background region finally is given by the intensity relationship multiplied by $\sqrt{(2\ell n 2)}$

$$t_{max} \sim 1{,}177 \frac{7{,}36\times10^{-3} - 3{,}84\times10^{-6}*\Gamma_n}{1{,}13\times10^{-3} + 1{,}33\times10^{-6}*\Gamma_n} \qquad 9.6$$

9.3 Two- and pseudo-two channel analysis

In Table 9.2 t_{max} is given at various resolutions. For two-channel evaluation the optimum position of the inner discriminator from Figure 6.6b is seen to be for this limited range of t_{max} and R ~ 0,1 at about 1,36 σ, which corresponds to a convenient setting at full width 40% peak height (i.e.FW4/10M) of prominent gold Kβ' peaks. The FW4/10M positions of six discriminators A to F for two channel evaluation of the gold Kβ' peaks are shown schematically in Figure 9.1. Counts from the two peak regions BC and DE are summed into one counting channel and AB + CD + EF into the other. In pseudo-two-channel evaluation, two discriminators each would be required for B, C, D and E, all in all ten discriminators instead of six.

Also shown in Table 9.2 are the standardised two-channel and pseudo-two-channel variances from Figures 6.6a and 6.7a for R = 0,1. In the double β' peak evaluation the variances or measurement times with a two-channel scheme are only 3 to 8% higher than with a pseudo-two-channel scheme at a saving of four discriminators in ten. An approximate comparison of the pseudo-two-channel evaluation for only the $K\beta_1'$ peak and the two-channel evaluation for both Kβ' peaks shows that the two-channel scheme would increase the measurement time per peak by about 7%, but this is more than compensated for by the 9/35th additional information contributed by the Au $K\beta_2'$ peak; the latter scheme thus permits at least 13% (i.e. 9/(35 + 9) - 7%) faster measurement with the same number (6)

Table 9.2 Spectral region and variances in gold ore analysis at various system resolutions

Γ(ev)	$t_{max}(\sigma)$	$2_V B$	$2{:}3_V B$
400	7,7	11,0	10,4
450	7,7	11,4	10,7
500	6,5	11,8	11,0
550	6,0	12,2	11,3
600	5,6	12,7	11,7
650	5,2	13,2	12,2
700	4,8	13,8	12,7

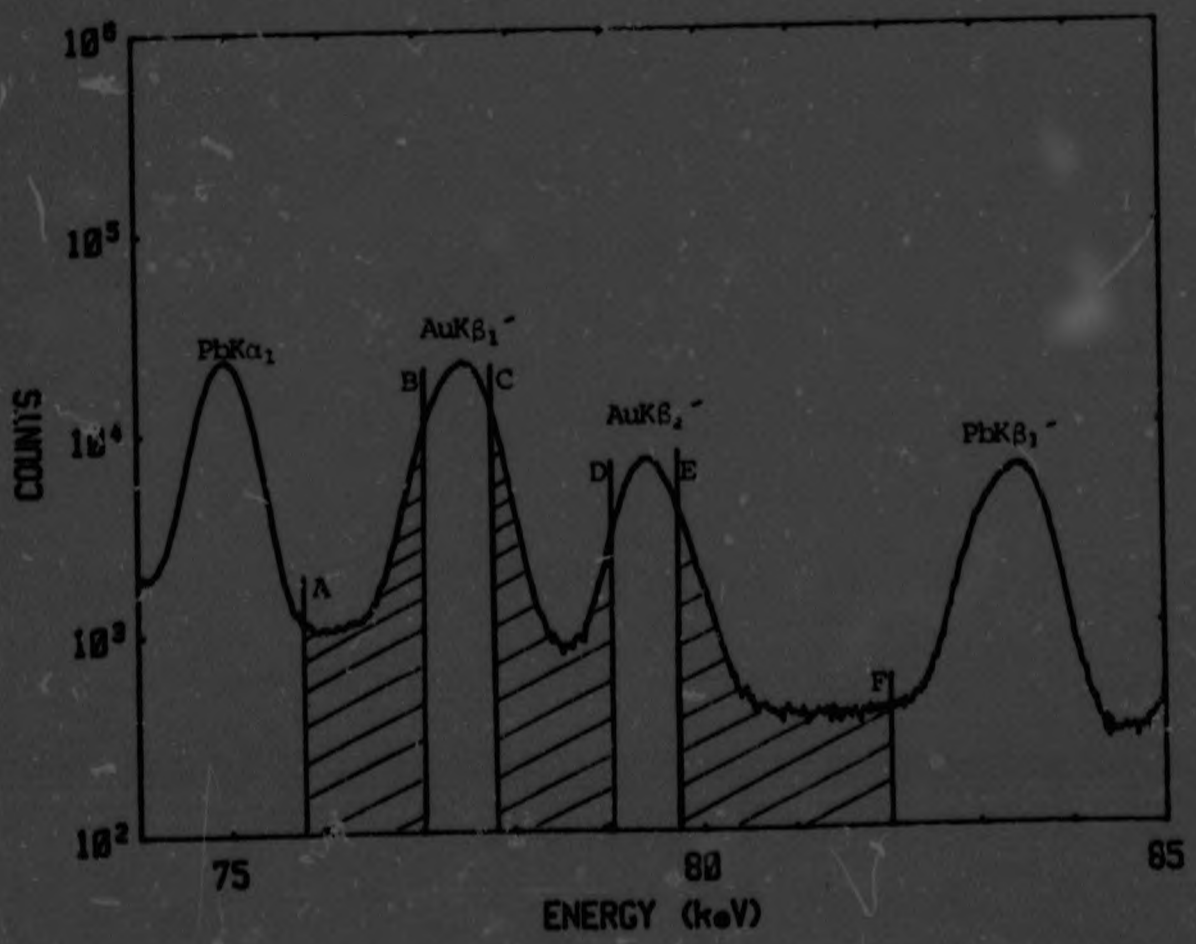


Fig. 9.1 Discriminator positions for two channel evaluation of gold $K\beta'$ peaks

of discriminators.

From the above treatment it may be concluded that with six discriminator, two channel evaluation of both the Au $K\beta_1'$ and Au $K\beta_2'$ peaks is an optimum scheme for gold ore analysis with a simple field instrument. This is only 16% slower than is theoretically feasible with multichannel, weighted least-squares Gaussian evaluation.

9.4 The peak-to-background ratio detection limit

The variable parameter in the previous section, the system resolution Γ, is a function of the amplifier time constant TC. Longer time constants give better energy resolution but lower signal processing efficiency P. A combination of parameters is, therefore, sought which allows the shortest measurement time T_m for a specified precision.

At a given detector count rate, r, three factors varying with Γ influence the required measurement time T_m - the standardised variance V^B, the specified peak-to-background ratio R and the signal processing efficiency P.

A detection limit for a peak-to-background ratio of R = 0,1 may be provisionally specified at the fundamental peak resolution (Γ_n=0). If, according to Currie (1968), for 5% errors of the 1st and 2nd kind a 1,65 S.D. critical level and a 3,29 S.D. detection limit (i.e. coefficient of variation CV=1/3,29) is adopted, then the variance in R of a measurement at the limit has to be

$$V = (R \times CV)^2 = (0,1/3,29)^2 = 0,00092 \qquad 9.7$$

In the two-channel evaluation the standardised variance (B=1) at the fundamental resolution (for which t_{max}=7,7σ) is

$$0,1^2 V^B_{7,7} = 11,0$$

The 2σ background count (for 2 sided evaluation) thus ought to be

$$B = V^{B}/V \qquad 9.8$$

From equation 9.5c the 2σ relative intensity in the spectrum of Figure 4.1 is

$$(r_B/r) = 1{,}13\times10^{-3}/\sqrt{(2\ell n2)} \sim 9{,}6\times10^{-4} \qquad 9.9$$

The total analysed count required for the specified detection limit (R=0,1 for Γ_n=0) is therefore

$$\frac{r}{r_n}\left(\frac{V^B}{V}\right) \text{ counts} \sim \frac{1044}{0{,}001} V^B \text{ counts}$$

$$\sim 939600 \times V^B \text{ counts} \qquad 9.10$$

As the resolution gets poorer the peak intensity remains constant giving a smaller but wider peak, the background intensity per unit energy remains unchanged, but the intensity per peak resolution increases so that the peak-to-background ratio decreases. For the gold Kβ′ peaks the increase is proportional to the value given in equation 9.5c and the detection limit ratio can be specified at any resolution as

$$R = 1{,}13\times10^{-4}/(1{,}13\times10^{-3} + 1{,}33\times10^{-6}\Gamma_n) \qquad 9.11$$

The different R's correspond to the same gold concentration and if the CV of the measurement is to remain constant (at 1/3,29) then, according to equation 7.3, the total analysed count (eq. 9.10) has to be increased by 0,1/R.

At a detected count rate r the total analysed count is given by rT_mP where T_m is the measurement time and P the signal processing efficiency. The measurement time to accumulate the required number of counts at the specified detection limit is therefore

$$T_m = \left(\frac{r}{r_\beta}\right)\frac{1{,}1V^B}{rPRV} \qquad 9.12$$

The signal processing efficiency in single element analysis is

$$P = \mathrm{Exp}(-rw) \qquad 9.13$$

where w is the effective pulse width (chapter 8) usually measured in system time constants TC. In efficient signal processing systems typically $w \sim 5,5TC$ or even smaller, but in less efficient systems w can readily exceed 12TC. The resolution Γ of a system depends mainly on TC and not on the factor w/TC. In Table 9.3 the system resolution (at 80 keV) and TC are given for a typical 200mm^2 germanium detector, and P has been calculated for a total detected rate of r = 50 kHz which amounts to a detected flux of 25 kHz/cm^2. The ratio R and $^2v^B_{t_{max}}$ in Table 9.3 were calculated from equation 9.11 and were taken from Table 9.2. The time

Table 9.3 Data acquisition parameters for gold ore analysis for a typical 200m^2 Ge detector at r = 50 kHz

Resolution Γ(eV)	TC μs	P=Exp(-rw) w=5,5TC(12TC)	Limit R	$^2R^vt^B_{t_{max}}$	T_m(s)
400	—	—	0,1	11,0	—
450	2,8	0,46(0,19)	0,094	11,4	589(1467)
500	1,1	0,74(0,52)	0,089	11,8	402(573)
550	0,65	0,84(0,68)	0,085	12,2	385(477)
600	0,42	0,89(0,78)	0,081	12,7	396(455)
650	0,32	0,92(0,82)	0,077	13,2	421(468)
700	0,24	0,94(0,87)	0,074	13,8	451(488)

required to measure the specified R with a CV = 1/3,29 at r = 50 kHz calculated from eq. 9.12 is shown in the last column of the table and in Figure 9.2.

A minimum measurement time of T_m = 385 (455) seconds is indicated for the specified ratio detection limit at a system time constant of TC = 0,6 (0,4) μs.

9.5 System time constant and detector size

Similar calculations were performed for some larger and smaller planar detectors at a flux of 250 Hz/mm^2. The noise resolution (in eq.9.1a or b) was assumed to be directly proportional to the detector capacitance of 22,5 fF/mm^2 plus a stray capacitance of 5pF as discussed in chapter 5.2.1. The measurement times for the specified ratio detection limit (eq.9.11) are shown in Figure 9.2 and the minimum values are reproduced in Figure 9.3.

Figure 9.2 shows that the minimum measurement times at a total count rate of 250 Hz/mm^2 are attainable at TC $\sim$ 0,6μs for a wide range of detector sizes.

The measurement times for the specified ratio detection limit are inversely proportional to the detector size when the size is small but above 100mm^2 poorer resolution and lower signal processing efficiency counteract this trend. In Figure 9.3 the lowest measuring time of 293 seconds is shown for a 400mm^2 detector running at 100 kHz. The measurement time required with a 200mm^2 detector at 50 kHz is, according to this analysis, $\sim$ 30% higher than the minimum attainable with the larger detectors that cost disproportionately more. In most signal processing systems, however, count rates as high as 100 kHz would cause resolution degradation in

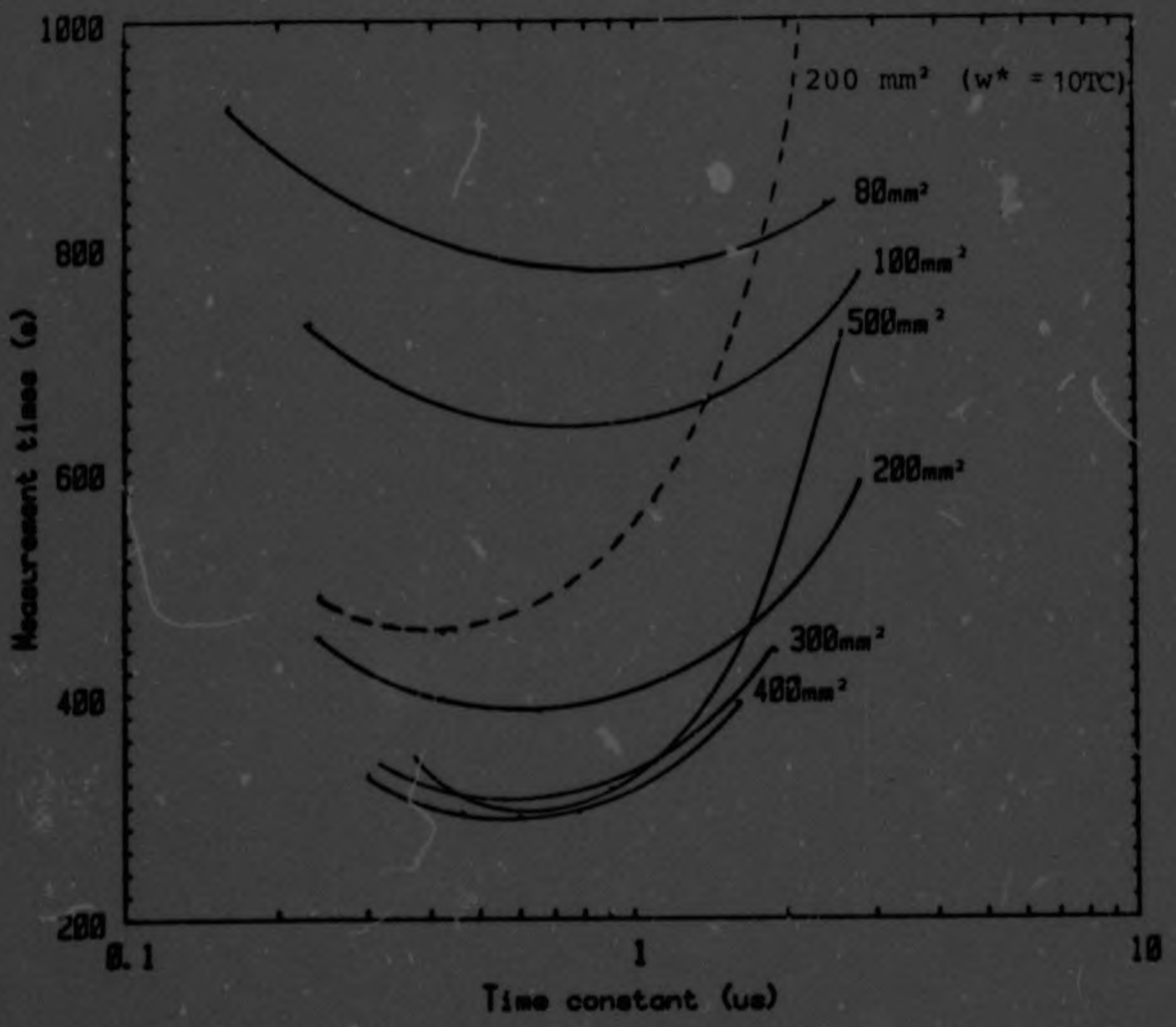


Fig. 9.2 Measurement times for specified ratio detection limit vs. TC for various detector sizes ($w^* = 5.5TC$).

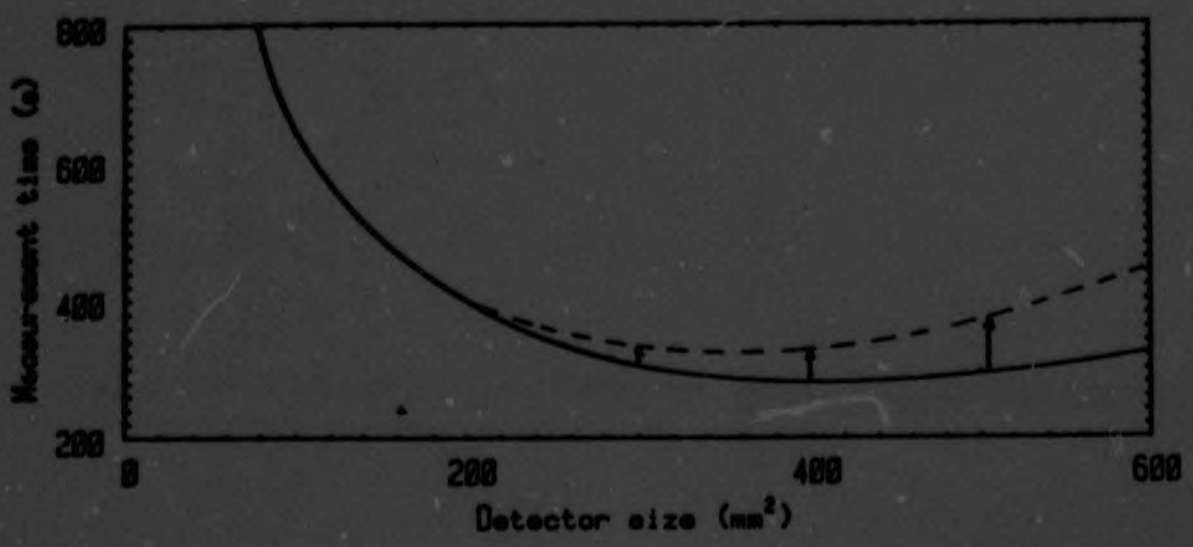


Fig. 9.3 Measurement times @ 250Hz/mm^2 vs. detector size

addition to the capacitance noise contribution already taken into account. This would increase the minimum measurement times of the larger detectors as indicated by the arrows in Figure 9.3, shifting the lowest point of the curve to smaller sizes.

This analysis has shown that a germanium detector size of 200mm^2 (a standard size in the industry) would be optimum for the measurement of gold ores.

9.6 The gold concentration detection limit

The ratio detection limit provisionally specified in section 9.4 (eq. 9.11) can be related to a certain gold concentration. Absolute derivation of the relationship from fundamental parameters is beyond the scope of this thesis as the differential scattering cross sections are not readily available. An empirical determination of the concentration detection limit follows below.

A powdered ore sample assaying approximately 400 p.p.m. gold was measured with a 200mm^2 Ge detector and a system time constant RC= 0,5 μs at r = 50 kHz. The total gold $K\beta_1'$ and $K\beta_2'$ peak counts above the interpolated background were determined as 58500 + 19200 = 77700 counts. The FWHM resolution of the system at 80 keV and 50 kHz was determined as 600eV, and from eq. 9.3, $\Gamma[\beta_1'] = 800eV$ and $\Gamma[\beta_2'] = 660eV$. The interpolated 1σ (i.e.Γ/2,355..) background counts were 27000 and 12000 respectively totalling 39000 counts. The peak to background ratio determined for 400 p.p.m. was therefore 77700/39000 = 2,0. The detection limit ratio specified by equation 9.11 and the parameters in Table 9.3 thus correspond to a concentration detection limit of (see

5th row of Table 9.3) -

400 x 0,081/2,0 = 16 p.p.m. gold

and a measurement S.D. = 5 p.p.m. gold.

With a 200mm^2 Ge detector and an efficient signal processing system (w = 5,5TC) this limit can thus be measured in 385 seconds at a count rate of 50 kHz. For single measurement times up to a few hours, at this count rate, the detection limit is inversely proportional to the square of the measurement time, beyond this, long-term instrument instabiliy may result in measurement standard deviations that exceed these lower standard deviations derived from counting statistics alone.

9.7 Discussion

The values of several of the parameters used in this chapter were decided on from measurements with systems differing appreciably from an optimised system for gold valuation. They served to illustrate the procedure of arriving at optimised conditions, but they may be revised as the optimising criteria can be more precisely defined.

The choice between Cd-109 and other isotopes rests mainly on the need for rapid measurement of very low concentrations. If measurements are not performed in situ then slower measurement might be acceptable and a less costly isotope might suffice.

The choice of the energy region is determined by the occurrence of interfering elements in the ore. The decision to include the Au $K\beta_2'$ peak in the evaluation was made in the interest of faster measurement, as it does not involve additional instrumental complexity.

The reason for optimising the evaluation for peak to background ratios below 1 is that for gold ore valuation the measurement of low concentrations, particularly of marginal grades, is considered more important than that of high concentrations. Ratios as high as R = 10 can be expected occasionally, but even their non-optimised evaluation would furnish a measurement precision in excess of requirements. The optimum precision to which an individual sample needs to be measured will depend on the use to which the measurement is put, and will be discussed in the next chapter. The detection limit of 16 p.p.m. in 385 seconds, arrived at in the previous section, can, by means of equation 7.3, readily be adjusted to any particular need, probably as low as fractional parts per million.

A count rate of 50 kHz average was assumed from estimates of the count-rate handling capability of a number of commercial systems. This rate, i.e. 250 Hz/mm^2, received in a 200mm^2 detector from a fluoresced sample 50mm away, gives an acceptable radiation dose rate at approximately 125mm behind the detector where a portable probe would be held. If this dose rate is not to be changed, then the count rate for different size detectors must be proportional to their area. However, the optimum sample distance depends to some extent on the thinness of the tabular deposit and the count rate would change considerably with a small adjustment of the measuring distance without a significant change in dose rate. It may thus be advisable to operate at a different count rate, most probably at a higher rate, depending on the types of deposit encountered.

Examination of Table 9.2 shows that an adequate interference- free region is available for evaluation of the gold Kβ´s. The change in t_{max} with resolution is associated with a moderate linear change in the standardised variances. In Table 9.3 it can be seen that the latter change is slightly smaller than the change of the composite ratio of the Kβ´ peaks and background. The exponential change in signal processing efficiency has a similar but opposite effect on the measurement time and this time thus has a pronounced minimum in the resolution range considered.

Comparison of an efficient signal processing system (TC/w = 5,5) with a less efficient system (TC/w = 12) in Table 9.3 shows that optimum measurement times are about 455/385 i.e. 18% longer with the latter system. It is possible to obviate this increase by careful design based on thorough understanding of the processes involved. The concept of pileup overlap parameters evolved in this thesis has greatly facilitated this. At lower count rates there would be less of a difference in measurement times, but at the more probable higher count rates the difference increases sharply.

In this chapter it has been shown that for in situ gold ore measurement a two channel scheme for the evaluation of the minor gold $K\beta_1'$ and $K\beta_2'$ peaks on the scattered background ensures good efficiency with an uncomplicated instrument. A $2cm^2$ detector and efficient signal processing at a time constant of TC = 0,6μs permit optimum measurement times at a constant detector flux. At 250 Hz/mm^2 the (3,29 S.D.) detection limit is 16 p.p.m. gold in a measurement time of

385 seconds. This limit is inversely proportional to the square of the measurement time and the square of the count rate.

10 QUANTITATIVE MEASUREMENT OF ROUGH ORE SAMPLES

In Chapter 4 consideration was given to the source-sample-detector geometry. In this chapter the geometry of the sample itself is considered. Geological samples normally require preparation before quantitative analysis, typically homogenisation of the sample and presentation in a reproducible measuring geometry. Such preparation is not feasible where mine stope faces are to be scanned for gold ore valuation. The samples, i.e. the areas on the face to be measured, have a rough surface, particularly in the gold containing regions where the rock may be more friable than in the waste rock above and below the reef.

Furthermore, the thin layered, sedimentary nature of the deposits requires that the area concentration of gold in g/m^2 (or related units) instead of the volume concentration in g/m^3 be determined. Accordingly it is necessary to determine the area concentration by viewing the layered deposit edge on, which is a difficult sample shape for quantitative measurement because of its heterogeneous nature.

10.1 Homogeneous concentrations

In the laboratory, where a constant measuring geometry can be assured, absolute counting of the gold peaks plus their background would give a quantitative measure of the gold concentration in homogeneous samples. Alternatively at variable count rates the counting of the gold peaks plus

their background relative to the easily measured Compton peak would give a quantitative measure.

Because the detected count rates vary approximately as the inverse square of the radiation path length, absolute counting of the gold peaks plus background would not be a quantitative measure. Moreover, for rough surfaced samples the finite dimensions of source and detector and the comparatively short radiation path lengths result in a backscatter angle at the sample from source to detector which is significantly smaller than 180°. With a smooth surfaced sample this angle may be held constant, but with a rough sample it varies with changing radiation path lengths. As shown in chapter 4 the background under the gold peaks is influenced by this angle. For rough surfaced samples the Compton peak and the background under the gold peaks, therefore, do not have a high enough correlation for the quantitative determination of very small gold peaks by the relative counting of these peaks.

The background adjacent to and between the two gold $K\beta'$ peaks is, however, well enough correlated with the background under the peaks for the determination of very small peak to background ratios even if the radiation path length and scatter angle vary appreciably.

Over the limited energy region from the lead $K\alpha_1$ peak to the lead $K\beta_3$ peak the mass absorption coefficient of the rock matrix decreases by about 15% but the mean mass absorption coefficient of the background energy regions adjacent to and between the gold $K\beta'$ peaks hardly differs from the mean mass absorption coefficient of the two $K\beta'$

peak energy regions. With the same entrance and the same exit absorption coefficients, the singly scattered background photons thus follow the same radiation paths i.e. the same sample depths as the exciting and fluoresced photons.

The multiple scattered background photon follow slightly different radiation paths but they constitute only a small proportion of the total scattered photons.

The nett gold peaks and the regional background thus come from the same sample and, therefore, their ratio is a good measure of the gold mass concentration.

Because different parts from the sample contribute different proportions to the total detected intensity the (unweighted) ratio of gold to background is a measure of concentration only for a homogeneous sample. If the mean radiation path lengths vary greatly while scanning rough surfaces, the relationship between the ratio of gold to background and gold concentration may be poorer.

10.2 Thin layered sedimentary concentrations

The majority of the Witwatersrand gold deposits are thin, layered deposits. Although the 'reef' conglomerate may be several decimeters thick, the gold is often concentrated in a layer or layers less than 5cm thick, sometimes existing only between the contact of two sedimentary layers.

These deposits are mined edge-on, the complete thickness of the gold bearing layer being extracted with additional waste rock above and below it. For ore valuation the amount of gold per area mined needs to be determined, regardless of the thickness mined i.e. regardless of the stope 'width'.

...

The valuation unit most commonly used in the gold mining industry is the area concentration unit g/m^2 divided by the rock density (2,76)t/m^3 to give cm.g/t, or more rationally cm.g/t. The advantage of this area concentration unit is that the values for several layers are additive and that on division by the stoping height (in cm) it gives the extracted or mill mass concentration in g/t, or divided by the sample height gives the homogeneous or average sample mass concentration in g/t.

In the horizontal direction, or rather in the plane of the reef, scanning with the fluorescence probe effectively homogenizes a sample; however, normal to the reef plane a heterogeneous sample is seen by the probe. When the distance between the probe and sample surface increases the effective sample height increases while the effective sample depth decreases, i.e. more waste rock above and below a gold bearing layer is seen by the probe, and the measured concentration (in g/t) decreases.

A 1cm thick cemented ore slab having a homogeneous gold concentration was sandwiched between large blocks of waste rock to simulate a narrow reef. Edge-on measurements at various distances of the probe from this sample and at various distances of the probe axis from the centre plane of the slab are shown in Figure 10.1. These illustrate the substantial effect the measuring geometry has on the precision in the quantitative measurement of heterogeneous samples.

To prevent wide fluctuations in measured concentrations of the same sample the variation in distance between the sample surface and the fluorescence probe may be 'limited'

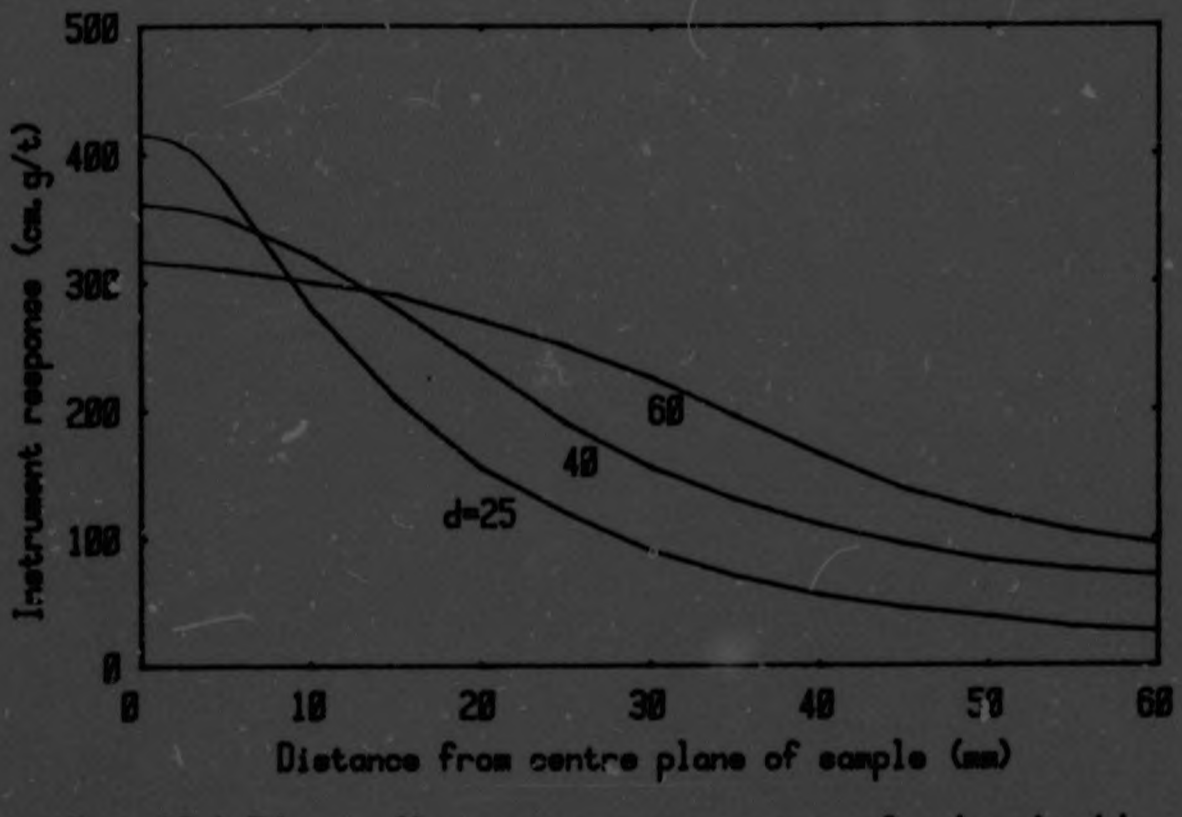


Fig. 10.1 Edge-on fluorescence measurements of a 'sandwich' ore sample; d = probe to sample distance (mm)

to a fixed range thus limiting fluctuations in the measured peak-to-background ratio from this source to acceptable values.

Restriction of short measuring distances to within a narrow range is mechanically not feasible on rough surfaces and another way was devised. It was found that the total count rate is inversely proportional to a low power ($\sim 1,4$) of the probe to sample distance. The count rate in the energy region between the Pb $K\alpha_1$ and $K\beta'_1$ peaks is a good measure of the distance to the centre of mass of the measured sample, but this rate is rather low. It was found that the total count rate above about 50 keV, which is far higher and therefore can be measured far more precisely over short periods, can give an accurate indication of the distance. In Figure 10.2 the regression of count rate and

probe-to-sample distance is shown, and the two standard deviation limits for measurements of five milliseconds are indicated.

In practice the effective distance was restricted by interrupting data accumulation for gold peak-to-background determination whenever the total count rate, measured with a ratemeter, fell outside two set count-rate limits. These count-rate limits could be chosen to correspond to limits in the probe-to-sample distance over which the maximum errors in a single measurement were acceptable. These limits would normally be ascertained from smooth-surfaced standard sandwich samples, but the somewhat larger variations in

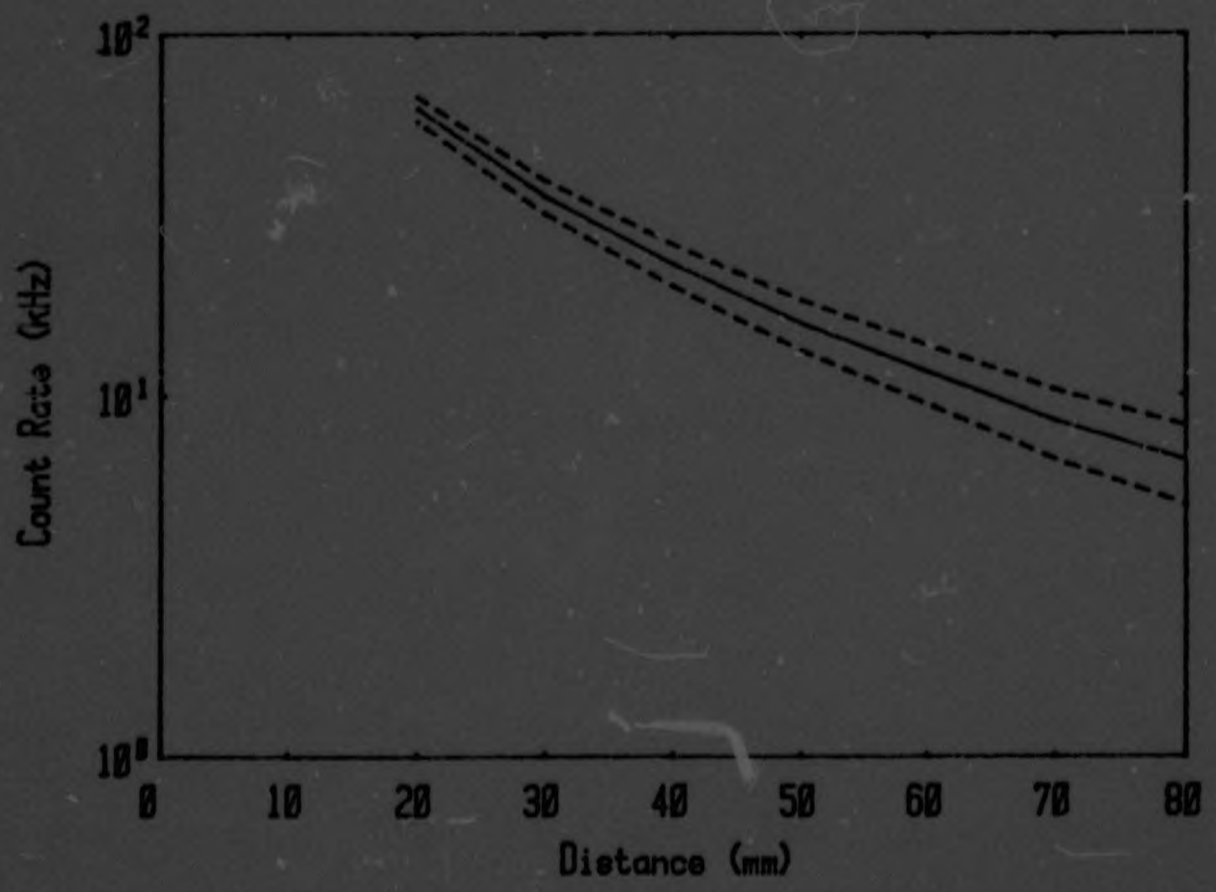


Fig. 10.2 Total count rate (>50 keV) vs. probe to sample distance; - - ± two st. dev. for 5ms

distance from particular small portions of rough samples needs to be taken into consideration in the final settings.

10.3 Shape of the fluorescence sample

The vertical profiles in Figure 10.1 reflect the effective sample shape in the determination of area concentration values.

With a co-axial source detector geometry a flat surfaced sample has a shape similar to that of a segment from a sphere. If the segment is viewed as a series of concentric shells, the different layers would contribute different proportions per unit (sample) mass to the measurement, i.e. the innermost layers, which are closest to the probe, have the highest measuring weight. With sources (or detectors) collimated to less than 2π steradians the edges of the deeper sample layers are truncated. With rough surfaces this layered sample is effectively distorted in the direction of the source radiation paths with slightly increased measuring weight being given to sample sections positioned closer to the source.

The effective sample depth is fixed by the sample's mass absorption coefficients for both the exciting and the excited radiation and these are constants for the relevant energies in the gold ore matrix. The sample depth, therefore, is a constant even if the sample surface is very rough. A constant area of the projected ore body is thus measured edge-on with a fixed depth vertical profile, as required for determination of area concentrations.

If the separation between the source and detector is small relative to their distance from the sample surface,

the line normal to the surface of the sample is an axis of sample symmetry.

So far calibration factors have been empirically determined with sandwich ore samples. More work still has to be done to calculate the sample shape for the conversion of mass concentrations to area concentration units.

11 INSTRUMENTATION FOR THE GOLD ANALYSER

11.1 Instrumental requirements

The main instrumental requirements were the following:

Portability even in difficult locations underground,

Radiation, cryogenic and electrical safety,

Simplicity of operation, and

Fast measurement of trace quantities.

- Portability - The gold analyser is by present day standards, a very complex field instrument that sometimes has to be operated under very difficult conditions. Packaging of the instrument presented a major challenge as ruggedness is essential for underground conditions. It was realized that several kilograms of instrumentation were involved. Since this weight cannot, for prolonged periods, be carried as a single package with an outstretched arm while scanning a stope face and crawling or crouching, it was decided to use a handheld measuring probe connected by cable to a chest pack (or back pack). The chest pack contains all the components that need not be in the probe so that the probe can be as light as possible. The lighter the probe the less it will tire the operator and the less inclined he will be to discontinue measuring or to scan inaccurately. The negatives are appropriate here as underground conditions make the operation strenuous.

- Safety - Aspects of radiation, cryogenic and

electrical intrinsic safety in explosive (methane) atmospheres were given careful attention from the outset of the project and are discussed in chapter 13.

- Operational simplicity - An instrument as complex as this could easily overwhelm an operator if he had to control a large number of the functions under mining conditions. During the development a method of operating the instrument was evolved by which the operator may focus all his attention in scanning the correct strata in the exposed mine face. Operational control for scanning was reduced to a single lever in the probe supporting grip. This lever allowed automatic sequencing of measuring and data storage, and actuated the source shutter and sample illumination light. Automatic storage in the instrument of all the day's data reduces drastically the amount of writing an operator has to do underground, and it eliminates human recording errors.

Control of the measurement during scanning is via a five digit LED display and a 9 LED bar on the front of the probe within the field of vision of the operator for almost any orientation of the probe. During measurement the 5 digit LED display functions as a 'Scan rate monitor' (displaying percentage of preset background counts) to assist the operator in maintaining a fairly uniform scanning speed parallel to the rock face. On completion of a measurement the measured gold value in calibrated units is shown on the display so that the operator can immediately base his valuation strategy on this value. On storage of the value the number of the measurement (from 0 to 255) is displayed

so that the operator may (occasionally) note down the correspondence between measurement number and the exact location in the mine, or record other comments on the measurement.

The 9 LED bar is a ratemeter display fuctioning as a probe-to-sample distance indicator. Should the distance be outside the range limits, the display flashes and data accumulation is interrupted.

The sample light and LED displays also serve as warning indicators for possible instrument malfuctions.

A great deal of effort by the manufacturer of the prototypes has gone into stabilisation of the electronic circuits so that the instrument will not require recalibration under widely varying, harsh conditions and over extended periods. Controls for (e.g. weekly) calibration checks are, however, accessible in the chest pack. High instrument stability greatly simplifies its operability.

- Fast measurement - Optimum parameters for efficient and high quality signal processing were discussed in previous chapters. The implementation of these parameters in some respects had to be compromised with limited battery capacity available in a portable field instrument.

11.2 Evolution of the instrument

The first experiments in the laboratory were performed with a 3mCi Co-57 source, a lithium drifted germanium detector with 30 litre cryostat and an amplifier plus multichannel analyser.

This developed towards 100mCi Cd-109 excitation, a

hyperpure germanium detector in a 3 litre omnidirectional cryostat which was portable although it weighed 11 kg. Pulsed optical feedback was used in the preamplifier. The amplifier incorporated pileup rejection and the amplified signal was analysed with three single-channel pulse height analysers in a pseudo-two-channel arrangement on the gold $K\beta_1'$ peak and two scalers.

Nuclear instrument modules (NIM) were used in a NIM bin with power supply. This was then housed in a box with self-contained air-conditioner and saturated core voltage regulation. This box, which weighed over 100kg, was then installed down a mine where it was installed near to a stope face. It had to be supplied, from a crosscut 300m away, with 3 KVA of 220 V single phase power from the mine's 550 V three phase network. This instrument is shown in Figure 11.1.

The first portable gold analyser consisted of a 1,5 kg probe with a liquid nitrogen holding time of about two hours and batteries, an analog board and a digital board in a 4 kg chest pack. A central 100mCi Cd-109 source was used and a $2cm^2$ x 7mm deep hyperpure germanium detector with resistive feedback in the preamplifier. The detector high voltage bias supply was housed in the probe. Liquid nitrogen in the probe had to be replenished from a portable dewar every one and a half hours and this caused many problems underground. Data stored in a solid state memory in the chest pack was printed out on surface after the end of each day's work. This instrument is shown in use in Figure 11.2.

The probe of the second prototype portable analyser was more ruggedly packaged and had a liquid nitrogen holding

time of six hours, adequate for one shift's work after filling on surface. Three sources averaging 40mCi each were used in a peripheral source geometry to permit an improved source shutter design and to allow source replacement by rotation. This geometry resulted in too high a scatter background from the protective cover that was used. In this prototype a multiplier was provided replacing one of two preset numbers thus providing a freer choice of calibration factors.

In the third prototype a central source geometry was once again used as the peripheral source geometry had resulted in an increase in measuring time for measurements of the same precision. The ruggedness of the probe had been further improved, operation had been simplified and the layout of the digital board was improved for production streamlining. In this last prototype version, visibility of the sample and the LED indicators was finally accceptable. This instrument is shown in Figure 11.3.

11.3 Components (block diagram)

Specifications for the third prototype of the portable gold analyser are given in a Chamber of Mines Research Report (LLoyd and Rolle, 1977), and these were presented to ORTEC INC. for implementation (Hill et al., 1978). Only the main components of the instrument are described below.

The instrument consists of a handheld probe assembly permanently connected by a short cable to a chestpack assembly, and an above-ground support module.

The analyser was separated into a probe and a chestpack to reduce the handheld mass to the minimum necessary so that



Fig. 11.1 First modular analyzer for in situ analysis



Fig. 11.2 First prototype portable analyzer in use underground



Fig. 11.3 Third prototype portable gold analyzer

the operational effort could be lightened. A pack worn on the back would have restricted crawling through narrow stopes. Complete, simplified operation of the source safety shutter and the functions of data accumulation, display and storage is controlled by a multifunction trigger in the probe handle. Two operational displays and a sample illumination light, multiplexed with warning signals, are strategically positioned on the probe. Protected controls on the chestpack serve only for calibration and 'On/Standby' switching of the instrument. The support module contains a battery charger, a readout module for the stored data, calibration support and a liquid nitrogen filling system.

An electronic block diagram of the analyzer is shown in Figure 11.4.

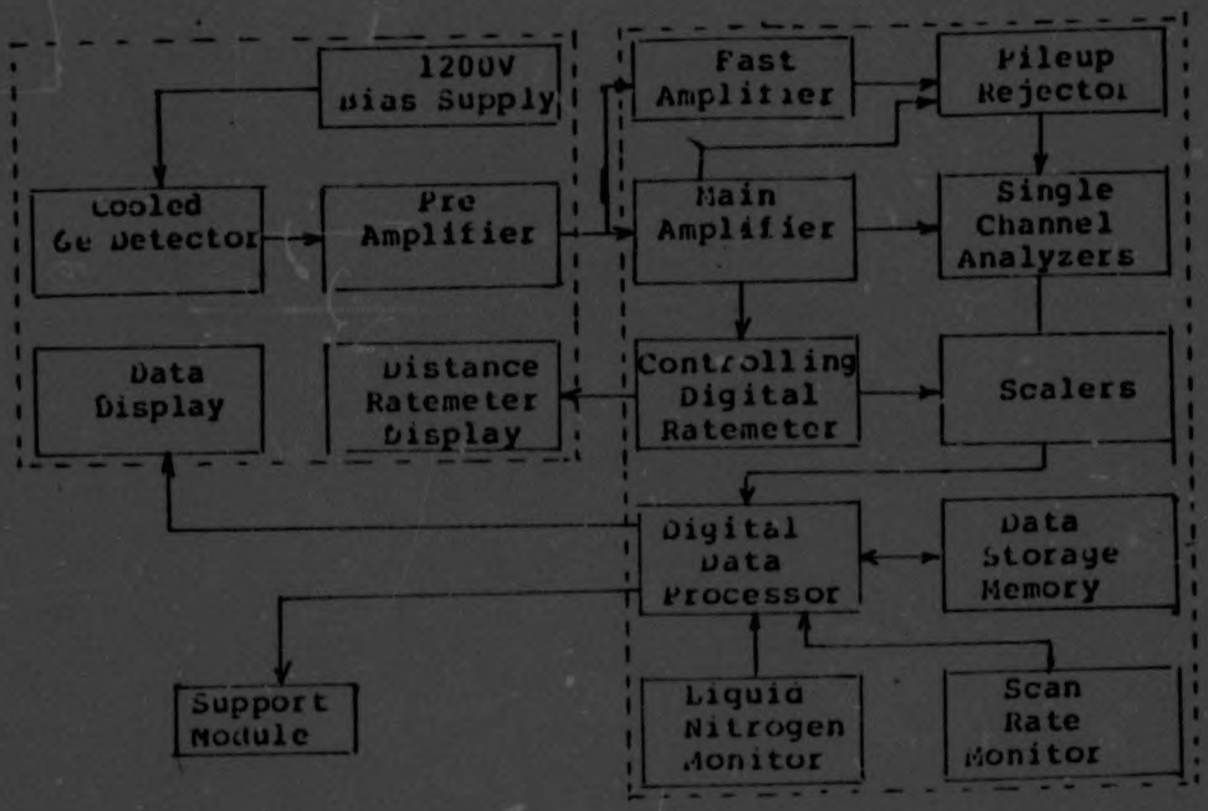


Fig. 11.4 Electronic block diagram of the third prototype portable gold analyzer

A miniature high voltage power supply in the probe provides the bias for the cooled Ge detector diode. The detector and the first stage of the preamplifier are cooled (to -196^{o}C) for high resolution. The preamplifier circuits are trimmed to allow count rates up to 500 kHz. The preamplifier and high voltage power supply are potted and all leads shielded or current limited to assure intrinsic safety.

The main amplifier uses a semi-Gaussian filter with a shaping time constant TC = 0,5us for good energy resolution consistent with the high count rates encountered in the measurement. The main amplifier pulse width w* = 5us, i.e. 10TC, and the leading edge of the pulse ℓ* = 1,4us i.e. 2,8TC. A gated baseline restorer is used and the baseline is monitored and the noise threshold automatically adjusted.

A fast amplifier, having a shaping time constant of 20ns, and a peak detector on the main amplifier output operate the pileup rejector. This has a pulse pair resolution time, p, of about 350ns, testing for pileup events greater than 6 keV.

A biased amplifier stage expands the region around 80 Kev to facilitate analysis by six pulse height discriminators. The output from these single channel analyzers to two scalers is gated by the pileup rejector and the distance controlling ratemeter.

The non-extending processing time of the analyzers $\ell^* = 0.25us$ concurrent with the trailing edge of the amplifier pulse. The leading edge overlap limit is thus also 0,25us. However the use of the peak detector results in a trailing edge pileup overlap limit equal to ℓ^*, i.e. $\beta = 1,4us$.

The total count rate above 50 KeV is measured by the digitial ratemeter every five milliseconds and displayed at the probe by a linear array of nine light emitting diodes to indicate the probe to sample distance.

The digital data processor converts the scaler contents to units of area gold concentration for display at the probe and for storage in a solid state memory, which can retain the results from 256 measurements. A preset timer monitors the holding time of liquid nitrogen and shuts off the 1200 V bias supply to the detector after a preset time to protect the cooled stage of the preamplifier.

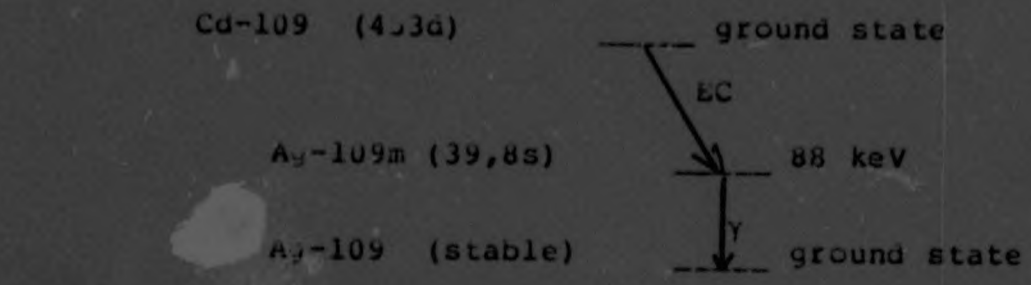
In the development of the portable gold analyzer several

high technology disciplines were brought together to solve a particular problem. A ruggedized hyperpure germanium detector, a small portable cryostat and high performance low power electronics adjusted to optimum parameters make this instrument possible.

High technology disciplines were brought together to solve a particular problem. A ruggedized hyperpure germanium detector, a small portable cryostat and high performance low power electronics adjusted to optimum parameters make this instrument possible.

12 CADMIUM-109 SOURCE AND COLLIMATOR

The decay scheme for 453d Cd-109 is as follows -



Cadmium-109 decays by electron capture to Ag-109m yielding 67,7% 22 keV silver K X-rays. This, in turn, decays with a 39,8s halflife to the ground state of Ag-109 by emission of 88 keV gamma rays. Approximately 96,4% of these are internally converted with a 34.6% yield of silver K X-rays; only the remaining 3,8% of the 88 keV gammas are useful for gold K level excitation.

A small source of about 100mCi (3,7 GBq) of Cd-109 is required in the instrument for gold valuation.

The source is a rather critical component. Its design was optimised so as to make efficient use of costly activity, at the same time reducing the potential radiation hazard and producing a source that can be handled safely underground.

12.1 Production and specific activity of Cd-109

Cadmium-109 is one of about twenty known isotopes of cadmium, eight of which are stable. Table 12.1 lists various

Table 12.1 Isotopes relevant in the production of Cd-109

Isotope	Halflife or nat. Abundance	Reaction	Remarks
^{107}Ag	51,82%	$(\alpha,pn)^{109}Cd$	cyclotron production
		$(\alpha,2n)^{109}In \longrightarrow ^{109}$	cyclotron production
		$(n,\gamma)^{108}Ag$	
^{108}Ag	2,4m	$\xrightarrow{\beta^-} {}^{108}Cd(n,\gamma)^{109}$ (96%); $\xrightarrow{\beta^+} {}^{108}Pd$ (4%)	reactor production
^{109}Ag	48,18%	$(d,2n)^{109}Cd$	cyclotron production
		$(p,n)^{109}Cd$	cyclotron production
		$(n,\gamma)^{110m}Ag$	
^{110m}Ag	253d	$\xrightarrow{\beta^-} {}^{110}Cd$	radiochem. impurity & reactor production
^{108}Cd	0,88%	$(n,\gamma)^{109}Cd$	reactor production
^{109}Cd	453d	$\xrightarrow{EC} {}^{109m}Ag \xrightarrow{\gamma} {}^{109}Ag$	
		$(n,\gamma)^{110}Cd$	reduces reactor prod. specific activity
^{110}Cd	12,39%		
^{112}Cd	24,07%	$(n,\gamma)^{113m}Cd$	reactor produced
^{113m}Cd	13,6y		radioisotopic impurity
^{114}Cd	28,86%	$(n,\gamma)^{115m}Cd$	reactor produced
^{115}Cd	44,1d		radioisotopic impurity

Isotopes relevant in the production of Cd-109.

Cadmium-109 can be produced by the (n,γ) reaction of Cd-108, by the (p,n) or (d,2n) reactions of Ag-109, or the (α,pn) reaction or (α,2n) followed by β^+ decay of Ag-107.

Reactor production of radioisotopes is normally cheaper than cyclotron production, but the isotopes cannot, usually,

be produced carrier-free i.c. without other stable isotopes of the same element. A carrier-free activity is desirable to reduce the attenuation of the gamma flux by self-absorption.

Reactor production through thermal neutron irradiation of natural cadmium is very inefficient as Cd-108 is only 0,88% abundant in natural cadmium and has a thermal neutron cross section of only 1,1 barn. Furthermore low activities of 13,6y Cd-113m and 44,1d Cd-115 would be produced as radioisotopic impurities, both emitting photons that would interfere with the spectrum from Cd-109.

The activity produced may be calculated as follows -

$$dN/dt \sim N\sigma\phi \quad (1 - 2^{-t/453d})$$

where N = number of atoms suitable for reaction

σ = cross section for Cd-109 formation

ϕ = particle flux

and the last term in parentheses being the saturation factor; the expression is not exact because subsequent nuclear reaction of Cd-109 and flux attenuation by the sample have been neglected. Substituting Avogadro's number, the natural abundance and atomic mass for N, the specific activity after 453d irradiation (half saturation) in a thermal neutron flux of $10^{14} cm^{-2}.s^{-1}$ is

$$[6,023x10^{23}x0,0088/112,4]x1,1x10^{-24}x10^{14}x0,5/3,7x10^{10} \text{ Ci/g}$$

$$= 0,070 \text{ Ci/g} \quad = 2,59 \text{ TBq/kg}$$

$$@ 8,65 \text{ Mg/m}^3 \text{ Cd} \quad = 0,61 \text{ mCi/mm}^3 \quad = 22,4 \text{ EBq/m}^3$$

The millimetre unit has been used for rationalization to source dimensions.

With highly enriched Cd-108 the specific activity could be increased by the relative abundance 1/0,0088 to 8,2 Ci/g

be produced carrier-free i.e. without other stable isotopes of the same element. A carrier-free activity is desirable to reduce the attenuation of the gamma flux by self-absorption.

Reactor production through thermal neutron irradiation of natural cadmium is very inefficient as Cd-108 is only 0,88% abundant in natural cadmium and has a thermal neutron cross section of only 1,1 barn. Furthermore low activities of 13,6y Cd-113m and 44,1d Cd-115 would be produced as radioisotopic impurities, both emitting photons that would interfere with the spectrum from Cd-109.

The activity produced may be calculated as follows -

$$dN/dt \sim N\sigma\phi \quad (1 - 2^{-t/453d})$$

where N = number of atoms suitable for reaction

σ = cross section for Cd-109 formation

ϕ = particle flux

and the last term in parentheses being the saturation factor; the expression is not exact because subsequent nuclear reaction of Cd-109 and flux attenuation by the sample have been neglected. Substituting Avogadro's number, the natural abundance and atomic mass for N, the specific activity after 453d irradiation (half saturation) in a thermal neutron flux of $10^{14} cm^{-2}.s^{-1}$ is

$$[6,023 \times 10^{23} \times 0,0088/112,4] \times 1,1 \times 10^{-24} \times 10^{14} \times 0,5/3,7 \times 10^{10} \text{ Ci/g}$$

$$= 0,070 \text{ Ci/g} \quad = 2,59 \text{ TBq/Kg}$$

@ 8,65 Mg/m^3 Cd = 0,61 mCi/mm^3 = 22,4 EBq/m^3

The millimetre unit has been used for rationalization to source dimensions.

With highly enriched Cd-108 the specific activity could be increased by the relative abundance 1/0,0088 to 8,2 Ci/g

or 71mCi/mm^3.

Russell (1964) irradiated natural silver foil for a period of four years in a thermal neutron flux of $\sim 2 \times 10^{14} cm^{-2}.s^{-1}$ to produce enriched Cd-108 and Cd-109 by the reactions

$$^{107}Ag\ (n,\gamma)\ ^{108}Ag \xrightarrow[2,4m]{\beta^-} {}^{108}Cd\ (n,\gamma)\ ^{109}Cd$$

Burnup of the Ag-109 and of Cd-109 produced also stable Cd-110, Cd-111 and Cd-112. The specific activity reached was 1,6 Ci/g or 14mCi/mm^3 Cd.

Cadmium-109 sources having a Cd thickness greater than 0,1mm substantially self-absorb 88 keV photons and the above specific activities thus indicate 100mCi source areas of the order of 1cm^2 for reactor produced Cd-109.

The (p,n) and (d,2n) activation functions of Ag-109 have peak values of 0,36 barn for 10 MeV protons and 0,62 barns for 14 MeV deuterons respectively, while the (α,2n+pn) combined activation function peaks at 1 barn for 27 MeV alphas (Wing et al., 1962; Dimitriev et al., 1967). The natural-silver thick-target yields shown in Figure 12.1 were reported by Dimitriev.

The cyclotron at the Council for Scientific and Industrial Research in Pretoria can accelerate 0.5mA of 10 MeV deuterons to produce 2mCi/n with a natural silver target or 4mCi/n with enriched (>99%) Ag-109 (@ R52/g). The 2,2m (86 inch) cyclotron at Oak Ridge National Laboratory accelerates 1,2mA of 22 MeV protons to produce 9mCi/n with a natural Ag-109 target. Thus yields are in agreement with the values shown in Figure 12.1. In some particle accelerators silver beam stops behind thin targets yield low-cost Cd-109.

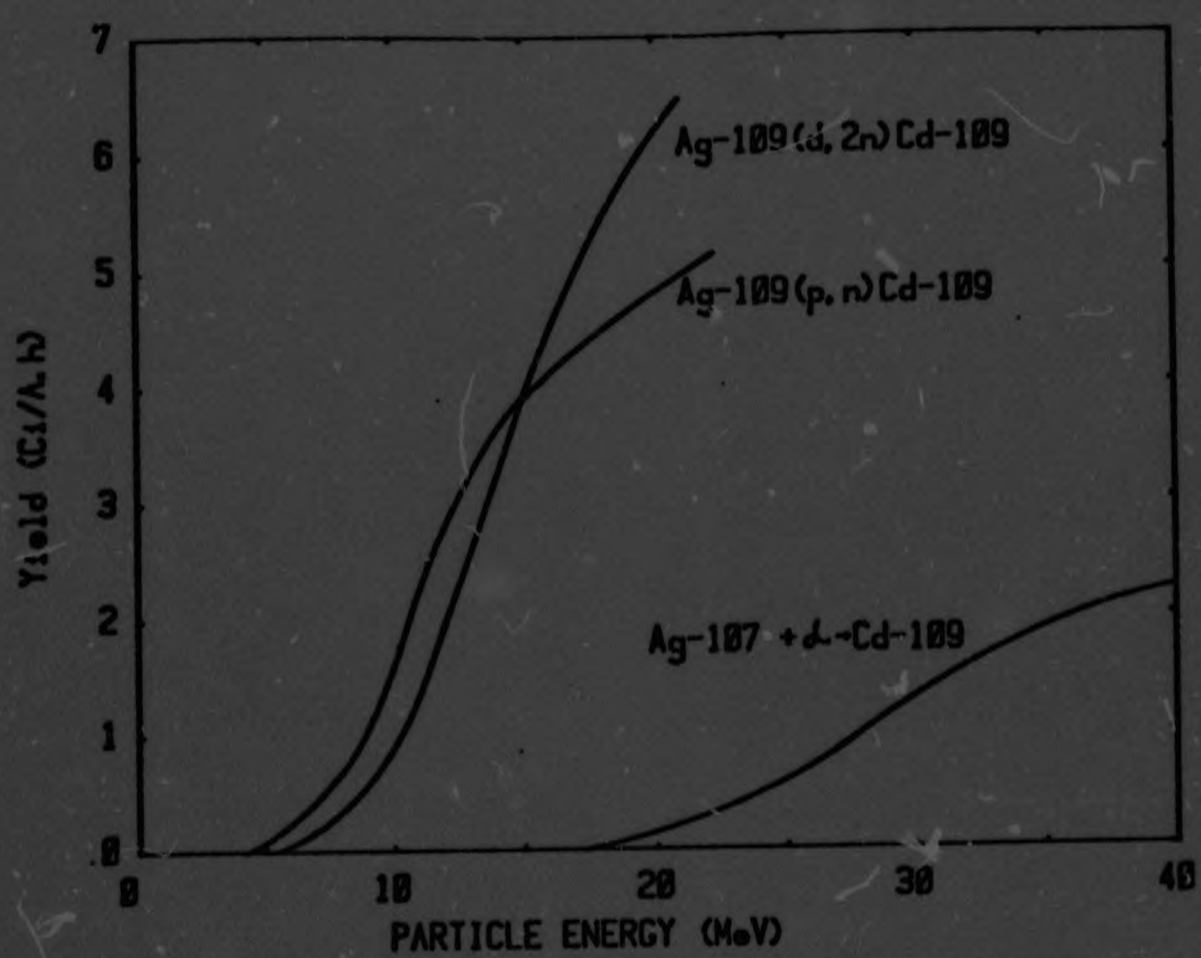


Fig. 12.1 Cyclotron production yield of Cd-109
(Dimitriev et al., 1967)

The specific activity of isotopically pure Cd-109 is

$$\frac{dN/dt}{N} = \frac{\ln 2}{453} \text{ disintegrations per day per atom}$$

$$= [6{,}023\times10^{23}/109] \times \frac{\ln 2}{453\times24\times3600} \times [1/3{,}7\times10^{10}] \text{ Ci/g}$$

$$= 2645 \text{ Ci/g}$$

$$= 22{,}9 \text{ Ci/mm}^3$$

In charged particle reactions some stable Cd isotopes are also produced. Trace amounts of cadmium originally present in a silver target and introduced during radiochemical separation may also reduce the specific activity slightly. Consequently the specific activity of the fresnly separated, carrier-free product does not normally exceed half the theoretical value and decreases as the Cd-109 decays.

The high specific activity of carrier-free Cd-109 has made possible 100mCi sources of less than 1mm² area without appreciable self-absorption losses of the 88 keV photons.

The Cd-109 may be radiochemically separated from irradiated silver targets. Russell (1964) used AgCl precipitation followed by chloroform/ pyridine solvent-extraction and Dowex 50-8X cation exchange. For carrier-free production, very high quality separation is desirable. Strelow (1978), after electroplating of the silver onto copper, separated the Cd in a nitric acid/ hydrobromic acid solution on an AG1-X8 anion resin.

12.2 Source and collimator design

The effect on gold measuring time of the photon scattering angle, from source to sample to detector, was discussed in section 4.3 and a central-source detector arrangement was found to be optimum. For this arrangement, shadowing of the detector demands that the source with its collimator be as small as practical. The minimum size of the source and collimator was limited by the available source manufacturing technology. With materials such as tungsten a shielding thickness of the order of 1mm was indicated and there would be little reduction in shadowing for sources smaller than 1mm diameter.

In the early stages of development difficulties were experienced by the C.S.I.R. in electroplating a nominal 100mCi activity of Cd-109 onto an area of about 1mm², but these problems were solved as the impurity levels in the Cd-109 plating solution were decreased. The integrity of the plated layer was improved and inactivation of the plated

surface by overplating with inactive cadmium or another metal, was considered for additional protection from possible exposure to corrosive atmospheres underground. Another metal would be preferable for overplating so as not to lower the specific activity for future recycling of partially decayed sources.

The low melting point of cadmium (321°C) presents a problem during the encapsulation of small sources by heat sealing methods such as welding.

At the start of the source development it appeared reasonable to use the radiation collimator with a suitable window for encapsulation of the electroplated activity, thereby eliminating additional encapsulating material which would increase the collimator diameter.

A molybdenum source window was silver-soldered into a tungsten collimator, the plated activity inserted and closed from the back with a tungsten screw which was cold-sealed with an inorganic thread sealant. Metal O-ring seals were also considered because in an earlier source, where the activity had been sealed from the front with an epoxied molybdenum window, the epoxy seal had undergone radiation damage and subsequently the source had leaked. The outside diameter (O.D.) of the tungsten collimator was 3mm, thus shadowing only 3.5% of a 200mm^2 detector.

Although it seems that all the source performance standards (ANSI, 1968) required for portable instruments could be met by the above integral source-collimator design, the reliability of the window seal and vibration and temperature classifications of the source (should the

instrument be left in a fire) were questioned by two commercial source manufacturers. A 2,5mm O.D. x 3mm long welded stainless steel capsule, meeting ANSI N5.10-1968 classification C33232,was thus developed as this type of design had been proven in the industry with existing source manufacturing technology.

Tungsten-inert-gas welding is used with the aid of a carbon block heat sink to prevent migration of the plated activity from the front of the source.

A 5,5mm O.D. tungsten alloy collimator was designed for the source capsule, shadowing 12% of the detector.

In figure 12.2 the source-detector arrangement used in the third prototype of the portable gold analyser is shown. The window and shield thickness derivations are given in the following sections.

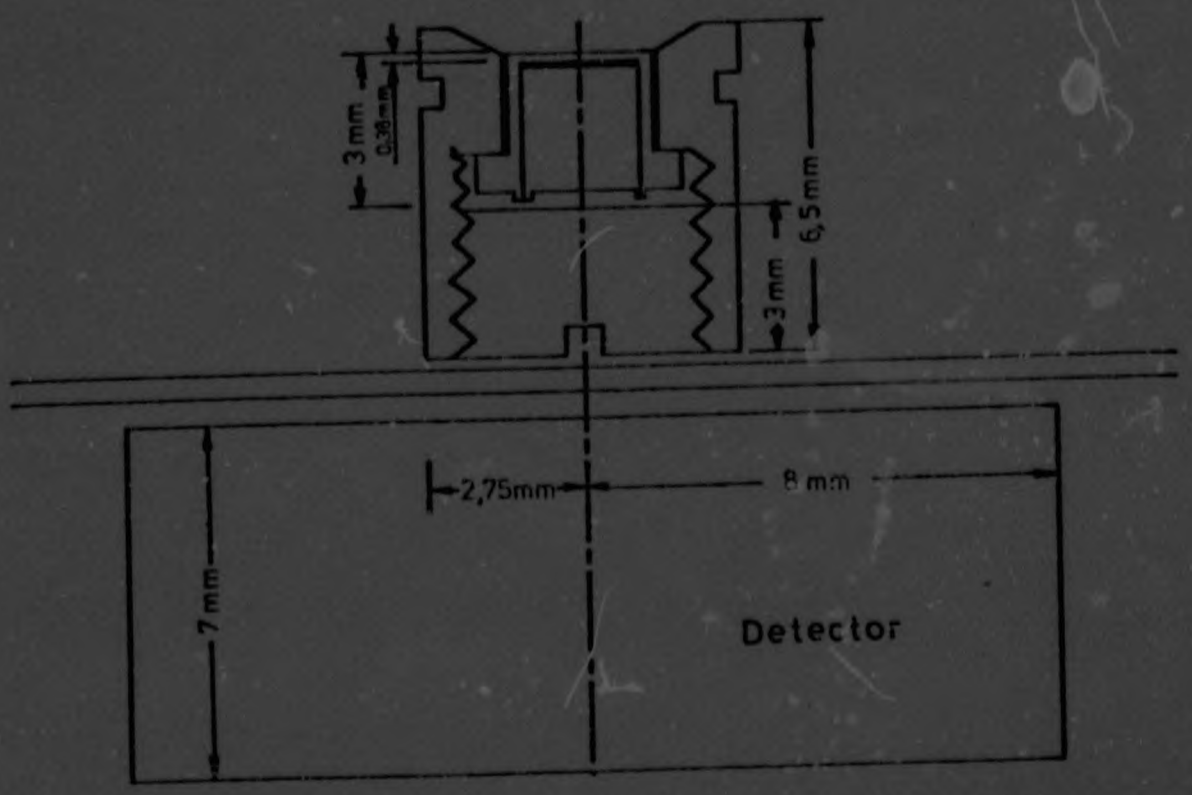


Fig. 12.2 Source detector arrangement in the third prototype gold analyzer

12.2.1 Source window

The window of the source was designed, in combination with the detector window, to filter out most of the unwanted low energy (22 keV) radiation with minimum attenuation of the useful high energy (88 keV) radiation.

The most suitable elements for filtration are those having a high mass absorption ratio for 22 keV and 80 keV photons. Elements Z = 22 to 43 (Ti to Tc) have mass absorption ratios between 40 and 47 while outside this range of atomic numbers the ratios fall sharply except for elements heavier than lead. There is little difference within this range of elements, so that iron with mass absorption coefficients of 25,0cm^2/g at 20 keV and 0,55cm^2/g at 80 keV is a convenient metal to use.

A thickness of d centimeters of stainless steel of density 7,86g/cm^3 reduces the ratio of 20 to 80 keV radiation intensity by the factor $e^{-7,86(25,0-0,55)d} = e^{-192d}$, where d is in centimeters. The intensity ratio of 22 keV to 88 keV radiation emitted by Cd-109 is 96,4/3,6 = 27. A ratio of the order of 0,01 is desirable at the detector so that the increase in total count rate from the low energy radiation may be insignificant. This requires a ratio reduction by about 2700 which is attained by a stainless steel filter of $(\ell n 2700)/192cm = 0,4mm$ thickness.

In the interest of reducing possible radiation exposure it would have been preferable to position most of this combined thickness at the origin of the radiation path, i.e. at the source window and to use the minimum thickness required for mechanical strength at the detector window.

The minimum detector window thickness allowed by the instrument manufacturer for an integral stainless steel-endcap of 41mm diameter was, however, 0,38mm. Consequently a thickness of 0,16mm stainless steel was allowed for the source window, in addition to the 0,38mm, to reduce the ratio in the open measuring field from 27 to 1,25, at which ratio the 22 keV radiation contributes less than 20% to the exposure in the external radiation field (see chapter 13).

The window thicknesses of 0,38mm and 0,16mm stainless steel attenuate the useful 80 keV radiation from the source to 85%x93%=79% at the detector. A 2,4mm thick protective polycarbonate cover ($C_{16}H_{16}O_3$) attenuates this still further at 94% to a rather poor 94% of 79%, i.e.74%. Any self-absorption in the plated activity attenuates the useful radiation still further; it is, therefore, important that all the Cd-109 be positioned against the source window within the shield's collimation angle.

The detector window causes the largest attenuation in useful radiation. A reduction in the presently employed thickness of 0,38mm stainless steel would increase the 85% transmission factor proportionately, without adversely affecting the detected spectrum.

12.2.2 Collimator shield

The purpose of the collimator shield is to reduce the direct radiation from the source to the detector to a level low enough not to cause interference in the spectrum from a sample. A forward collimation angle of 120° provides protection for the operator behind and to the side of the

probe.

The material used for the collimator needs to have a high linear absorption coefficient for photons of energies that might interfere in the spectrum; this applies not only to the 88 keV source radiation, but in particular to the X-rays generated in the shield, to which the shield is fairly transparent. A high linear absorption coefficient reduces the necessary size of the collimator thus shadowing less of the detector.

Several high density metals were considered for this application. Their absorption properties are listed in Table 12.2. Of these Ir, Pt and Au have Kβ X-rays in the

.able 12.2 Absorption properties of shielding metals (Berry 1962, Davisson 1968)

ELEMENT	DENSITY	MASS ABS. COEFF.		LINEAR ABS. COEFF.	
	g/cm^3	$\mu_{88}\ cm^2/g$	$\mu_{K\alpha},\ cm^2/g$	$\mu_{88}\rho cm^{-1}$	$\mu_{K\alpha},\rho cm^{-1}$
Ta	16.6	6,0	3,5	100	58
W	19,3	6,2	3,4	120	66
Re	21,0	6,4	3,3	134	69
Os	22,6	6,6	3,2	150	72
Ir	22,5	6,8	3,0	153	68
Pt	21,4	7,0	2,9	158	62
Au	19,3	7,2	2,7	139	52
Pb	11,4	7,8	2,5	89	29
U	19,1	3,7		70	

energy region between the Pb $K\alpha_1$ and $K\beta_1'$ lines and are thus to be avoided for gold determination. Metalworking of Os and Re is rather difficult, while the relatively low density of Pb and Ta gives these metals a correspondingly lower linear coefficient. Shielding by uranium is less because it does not offer K-level absorption of the 88 keV photons. Tungsten, or a heavy tungsten alloy which is more amenable to metalworking, is thus the shielding metal of choice.

The minimum amount of shielding may be calculated by stipulating that the constant intensity from the source directly to the detector should constitute only about one or two percent of the intensity from the sample at the limiting probe-to-sample distance.

The total count rate from a massive sample at a limit distance of 6,5cm from a 125mCi Cd-109 source and $200mm^2$ detector was determined to be 37,5 kHz.

The source radiation to be shielded may be considered as comprised of two components. The primary component is the 88 keV photons (of 3,6% abundance) i.e. $125x0,036x3,7x10^7=1,67x10^8$ photons/second emitted into 4π steradians. Since the mean range of 88 keV photons in tungsten is only $1/\mu_{88}\ \rho\sim0,1mm$, a secondary component of tungsten K X-rays is produced in the inner layer of the tungsten shield. The fraction of 88 keV photo-electric absorption, leading to W K-level excitation in a thick W target, relative to the total absorption (i.e. inclusive of incoherent scattering and L level excitation) is about 0,81 but only 0,94 of the excited W atoms produce K X-rays. With a $2\theta=120^o$, i.e. $\int_0^{\theta}2\pi\sin\phi d\phi=2\pi(\cos0-\cos\theta)=3,14sr$, forward

collimation angle of the shield, the shield intercepts $(4\pi-3,14)/4\pi=0,75$ of the primary radiation producing a secondary component of $1,67\times10^{8}\times0,81\times0,94\times0,75 \sim 0,95\times10^{8}$ W K X-rays per second emitted into 4πsr.

A detector of 8mm radius positioned 7mm behind a point source subtends a half angle of $\theta=\arctan(8/7)$ and a solid angle of $2\pi(\cos0-\cos\theta)=2,15$sr of the source. Thus a fraction $2,15/4\pi=0,17$ of the primary and secondary source components are directed at the detector. Equating the two components of the source radiation passing through the tungsten shield, of thickness d, to 1s (or 2s) of the intensity of the radiation from the sample, we have -

$$1,67\times10^{8}\times0,17e^{-\mu_{\beta}\rho d}+0,95\times10^{8}\times0,17\times e^{-\mu_{\chi}\rho d}= 0,01\times37500$$

giving $d \sim 1,6$mm (1,5mm for 2s)

The source backing thus ought to be 1,6mm thick while the oblique direction sideways through the shield requires only a $1,6 \times \arctan(8/7)=1,2$mm wall thickness. With heavy tungsten alloys these shielding thicknesses need to be increased by the ratio of the density of pure tungsten ($19,3 g/cm^3$) to the density of the alloy.

A wall thickness of 2mm and a backing thickness of 3mm in a W alloy of $18,2 g/cm^3$, formed by powder metallurgy, were provided by the instrument manufacturer. The increase in thicknesses from the minimum was arbitrarily provided to allow for undercuts in the shield wall for a source retaining collar and for secure molding into a polycarbonate cover, and for a slot in the W alloy screw in the shield backing.

The overall diameter of 5,5mm of this collimator with a

welded stainless steel source capsule results in a shadow area of 23,8mm^2 i.e. 12% of a 200mm^2 detector. With a smaller plated area of the Cd-109 activity and an integral source encapsulating shield this could be reduced to about 4 percent.

The relatively small improvements discussed in this chapter could all lead to a reduction in the amount of Cd-109 activity required to measure gold at optimum speed, and the radiation dose rate, to which an operator might be exposed, would be similarly decreased. However, it has essentially been found necessary to increase the Cd-109 activity in order to provide a safe means of securing the source while permitting its ready replacement.

13 SAFETY ASPECTS

The gold analyser presents three potential hazards, particularly since it is a portable instrument which is to be used under arduous conditions underground. These potential hazards arise from the use of liquid nitrogen as a coolant, the use of electronic circuits in atmospheres which may contain flammable or explosive gases such as methane, and the use of a radiation source.

13.1 Liquid nitrogen

High resolution germanium detectors operate at 77^{o} - 90^{o}K and usually are cooled with liquid nitrogen.

As an altenative coolant a solid-liquid propane system which could be completely contained (Boynton, 1974), was considered for this application. The latent heat of melting (80 J/g at 91^{o}K) is, however, lower than that of boiling liquid nitrogen (199 J/g at 77^{o}K) so weight and volume considerations favoured the latter. Lightweight (6 kg) mechanical refrigerators (Hogan, 1968; Carrol, 1971) operating on Sterling or Solvay cryogenic cycles were also investigated but their power requirements rendered them unsuitable for this portable application.

The potential hazards to the operator from liquid nitrogen are skin 'burns' from accidental contact with extremely cold surfaces or liquid and from the 174-fold volume expansion at the phase change which could cause

pressure problems in c ed systems.

Small droplets of liquid nitrogen when spilled onto the skin usually roll off and do not cause 'burns' unless they wet the skin.

To minimize the contact hazard, a spillproof dewar, which could be pointed in any direction, was specified. A design based on a commercially available, non-pressurized dewar was suggested; this had two vent pipes, at least one of which could always vent from above the liquid surface to the opposite outside without spillage, with minor restrictions on the orientation of the dewar. The instrument manufacturer simplified this to a single vent cum fill pipe terminating in the centre of a cylindrical dewar. In this design the dewar can be filled only to half the volume of the cylinder but it removes all restrictions on orientation of the dewar.

For handling of liquid nitrogen it is safer if the liquid need not be pressurized during transfer and use. Lightweight, quick-connect couplings for refilling of liquid nitrogen are prone to leakage due to cooling from ambient tempe. tures to below 80°K, and pressurization would aggravate this problem. Icing-up of the coupling can hardly be prevented when the weight of the probe has to be reduced to a minimum, but this inconvenience was found to be small for filling periods of less than an hour.

The diameter of the vent pipe was a critical parameter. For spillage during operation it ought to be small whereas for refilling a larger diameter is preferable, especially if the liquid has to run down the pipe with a counterflow of

displaced air and evaporated liquid. If two pipes to the centre of the cylinder were used the filling could be accomplished with smaller diameters than is needed for a single pipe. A single pipe, however, simplifies construction of the cryostat and a divider in the pipe was therefore suggested, which should allow some reduction in diameter as it separates opposing flows; with this design it has been possible to fill a warm probe, having a 3mm inside diameter fill tube, from a clip-on funnel within ten minutes.

For the first prototype portable analyser a liquid nitrogen holding time of one hour was specified, and the instrument manufacturer produced a probe with a holding time of nearly two hours. The refill system, which had to be carried underground, often failed as it could not stand up to normal underground treatment. For the second and third prototypes the liquid nitrogen holding time of the probe was increased to six hours, so eliminating the need to refill the probe underground.

If the probe of the fill system were pressurized with intermittent pressure release then there would always be the possibility that the pressure relief mechanism could ice up or fail otherwise and that vessels could rupture from pressure buildup. With an ambient pressure system the continuous boiling of the liquid nitrogen ensures that vents are continuously kept open so that ice cannot block the vent completely. Care must, however, still be exercised to keep water or ice out of the system during filling.

The small amount of liquid nitrogen required for operation thus need only be transfered above ground, and

handling there has been simplified so as to reduce potential hazards to a minimum. During filling of the large storage container it will be necessary to observe the simple precautions normally taken when handling potentially hazardous liquids. Underground the liquid is contained at ambient pressure in a spillproof dewar which presents no potential hazard unless the vent is blocked deliberately.

13.2 Intrinsic safety for fiery mines

The carbonaceous content of ores in some gold mines gives rise to methane (firedamp) which can present a potential explosion hazard. For these fiery mines instruments must either be encased in explosion-proof boxes, or they must be intrinsically safe, i.e. during operation or malfunctioning the energy in any spark that may be generated by the instrument must be less than that required for ignition of any methane-air mixture.

The armouring required for explosion-proof enclosures is incompatible with a lightweight, portable instrument. The remaining solution, intrinsic safety, had not been implemented on a related type of instrument before and presented a number of problems that had to be resolved in the design as discussed below.

The high-voltage bias supply (1200 V) for the detector was located in the probe and not in the chest pack so that energy storage in cables to the detector could be kept to a minimum; all circuits were resistively current limited and fuse protected at the nickel-cadmium batteries so that even short circuits could not produce energetic sparks; the incandescent sample light was specially enclosed to protect

it from external breakage. The possibility for tampering with the instrument was limited.

Aluminium and titanium were strong contenders for the probe vessel. However, when these metals are struck on iron oxides, widely present in a mine, the exothermic reaction can produce sparks and these metals were, therefore, avoided as structural materials. Cadmium also could not be used e.g. on plated screws. The fiery mine problem and corrosion problems underground made stainless steel the structural metal of choice.

After several consultations during the design stage the third prototype portable analyzer was submitted to the Explosives Hazards Division of the South African Bureau of Standards where it was tested and found to comply with the standard for intrinsically safe electrical apparatus (SABS, 1977). Approval was obtained from the Government Mining Engineer to use this prototype underground in Group 1 atmospheres, i.e. in the presence of firedamp.

13.3 Radiation safety

Approximately 4,6 GBq (125mCi) of Cd-109 in the gold analyser allow an acceptable measurement rate for ore valuation of narrow reefs. The potential radiation and contamination hazards from such a source thus had to be analysed.

Operator safety was carefullly considered in the instrumental requirements from the initiation of the design. This demanded that the activity should be used efficiently and as safely as possible. The following features contributed towards these objectives:

The source was designed to filter most of the unwanted 22 keV silver K X-rays with only a small reduction in the useful 88 keV radiation. A proven stainless steel encapsulation was used, and the source and collimator were securely and protectively mounted in the probe front cover to prevent damage to or loss of the source. A source-sample-detector geometry was developed which allowed a wide collimation angle for maximum use of the source, the close geometry enhancing the measurement of narrow reef bands. The detector size was made as large as resolution considerations permitted; the electronics were optimised to attain the highest practical rate of gold determination particularly at marginal gold values.

The nature of the measurement, i.e. backscatter scanning of extended rough rock faces, is such that it is impossible to contain the radiation within the system as can be done with a small sample which can be introduced into a systen. Reef scanning *in situ* requires good visibility around the probe head and as portable a probe as possible. The possibility of reducing the radiation by shielding was thus limited. The source is completely shielded to the rear and a close fitting tungsten shutter contains most of the source radiation whenever the operational trigger is released. A shutter lock was provided to prevent accidental opening. A light shining (at the sample) in the same direction as the source serves as a radiation warning; this light is switched on as soon as the shutter is opened.

Elaborate shutter systems had been contemplated, but it was realized that with this type of measurement a fail-safe

design is well-nigh impossible and could only give a false sense of security. A small potential radiation hazard should be considered present under all operating conditions. It can, however, easily be ascertained that the shutter is not damaged and is functioning correctly and whenever this is done the operator can rest assured that he receives no significant radiation dose when the shutter is closed. When not in operation, the probe can be clipped onto the chest pack where a lead cap over the source and shutter allows complete reliance on more than adequate shielding. Radiation warning lables are prominently displayed on the probe to discourage misuse or tampering.

Under normal operation the highest radiation dose rate would be received by the hand supporting the probe. In the first portable prototype the probe handle was near the front of the probe and the hand was shielded by a tantalum foil. In the second and third prototypes the handle was positioned under the centre of mass of the probe further back where the radiation intensity is less. The problem of accurately measuring dose rates close to low energy sources (<100 keV) is not simple and requires specialized equipment which was not available for this project. The radiation dose received by the hand can, however, be calculated from the blank backscatter spectrum shown in Figure 4.1 and the 50 kHz count rate received by the detector under normal operation.

The absorbed dose rate may be calculated from

$$\int_{>0}^{E_{max}} \text{flux(photons/h.mm}^2\text{)} \times \text{E(Joules)} \times \frac{\mu}{\rho}\text{(mm}^2\text{/kg)}\ \text{dE Gy/h}$$

if $\frac{\mu}{\rho}$ is the energy transfer coefficient for air (Davisson,

1968 p841), division by 0,877 will adjust the values to the absorption response of human tissue. The total photon flux of 50 kHz falls on 176mm^2 of unshadowed area of the detector, i.e. 1,02x10^6 photons/h.mm^2. The flux of photons of energy between E and E + ΔE may be calculated from the spectrum on Figure 4.1 -

$$1{,}02\times10^6 \; I_E\Delta E \; / \sum_{\cdot}^{88} I_E\Delta E \quad \text{photons/h.mm}^2$$

Approximate numerical integration over all energies gave an absorbed dose of 40μGy/h (4mrem/h).

For radiation calculations, at a nominal probe to sample distance of 40mm, the source may be considered as imaged 50mm behind the effective centre of mass of the sample 10mm deep in the rock, i.e. 100mm in front of the detector. The absorbed dose rate of 40μGy/h at 100mm may be converted to any position behind the shielded source by the inverse square distance relationship.

The fingers on the probe handle are positioned approximately 125mm behind the shielded source, and at that distance the dose rate is 40(100/225)^2 = 7,9μGy/h. The dose limit (IAEA, 1967) for the hand of individual members of the public, that need not be registered as radiation workers, is 75 milliGray per year (7,5rem/year). Under the most unlikely situation where an operator were to pull the probe trigger continuously for 40 hours per week, 52 weeks per year, the dose absorbed by his operating hand would be one fifth of the absorbed dose limit permissible for the public; if he were registered as a radiation worker the permissible limit would be still ten times higher.

The eyes cannot, normally, be closer than 300mm from the virtual position of the source in the rock opposite the probe, and at that distance the absorbed dose rate is 4,5 μGy/h. Since the permissible dose limit for the eye is five times lower than that for the hand, regular exposure of the most sensitive organ relevant in this application also does not give rise for the need to register the operator as a radiation worker.

For direct exposure to the 4,6 GBq (filtered, i.e.x0,038) Cd-109 source with the shutter open, the flux at 1m is

$0{,}038 \times 4{,}6\times10^{9} \times 3600 / 4\pi = 5\times10^{9}$ 88 kev photons/h.m^2

giving an absorbed dose rate of -

5×10^{10}(photons/h.m^2) x $88\times1{,}6\times10^{-16}$(J) x $2{,}66\times10^{-3}$(m^2/kg)

= 1,87 μGy/h (0,18mrem/h) at 1m

This rate has an inverse square distance relationship, for example, at 100mm from the source the absorbed dose rate is 187μGy/h.

It may be seen that continuous direct exposure close to the source may result in the permissible weekly absorbed dose being reached over a small part of the body within several hours. Operators of the instrument thus will be trained so that accidental direct exposure may be kept to a minimum. Notwithstanding the unlikelyhood of reaching the permissible absorbed dose for non-radiation workers, it is envisaged that operators will be registered as radiation workers and that routine personnel monitoring will be implemented.

From the above mentioned considerations it should be clear that all possible potential safety hazards have been adequately taken care of and are so small that they need not be of concern for general application of the gold analyser in the harsh mining environment.

14 RESULTS OF THE FLUORESCENCE METHOD

To test the feasibility of the method and to test instrumentation, a series of measurements had to be carried out underground. The first modular instrument was installed in a stope at Leslie Gold Mine Ltd.. The first prototype portable analyzer was tried on a number of panels at Marievale Gold Mine Ltd. and in an experimental stope at Blyvooruitzicht Gold Mine Ltd. Testing at this site continued with the second and third prototype analyzers.

14.1 Measurements at Leslie Gold Mine Ltd.

14.1.1 Equipment

The analyser consisted of an electronic package connected to a portable measuring probe by a 13m cable.

The package comprised a modular three-channel pulse height analyser with pile-up rejector and constant voltage power supplies, mounted in a temperature-controlled box. The box dimensions were approximately 0,6x0,6x1,2m and weighed about 100 kg.

The measuring probe consisted of a 100mCi Cd-109 radioisotope point source in a tungsten cup of outside diameter 3mm mounted concentrically 3mm in front of a 100mm^2 hyperpure Ge detector. The detector was cooled by liquid nitrogen held in a portable two-litre omnidirectional cryostat. An analog ratemeter functioned as an effective distance meter. The probe was tripod mounted and weighed

approximately 11 kg when full of liquid nitrogen.

14.1.2 Test site

The tests were carried out in the western area of the mine in stope 11A 28 Too on the two east panels adjacent to end-tipper track No.4.

Compared with samples from other parts of the mine, the values of chip samples from the western area, as revealed by repeat sampling of previous sampling channels, indicate a much larger scatter. Even though the ratio of projected sampled area to projected mined area of the reef in the western area was more than ten times greater than that for the rest of the mine, evaluation of the average grade of individual stope faces in the western area was more difficult than elsewhere in the mine.

In the test panels a single reef-band was located easily at the contact between the light-coloured quartzite hanging wall and the dark shale footwall. The thickness of the reef-band varied from a few centimetres to virtually zero. The surface of the face was particularly rough across the contact where the measurements were made. Steps of a few centimetres often occurred at the contact.

The stoping width ranged from 350mm to 1m, the dip was approximately at an angle of 20°, and the temperature 29°C dry-bulb.

14.1.3 Experimental

The electronic package and mains supply were installed in the end-tipper track for four weeks. The probe was filled daily with liquid nitrogen on surface.

At the beginning of each shift tests were made in the track for the presence of methane; as a further precaution a jet of compressed air was directed over the electronic package. The temperature controller was then switched on and the electronic calibration of the instrument was checked.

A continuous row of rectangles, 150mm wide and 80mm high (from 55mm above the contact down to 25mm into the shale) was marked along the face by a sampling official. Measurements were made centrally on both halves of each rectangle. The rectangles were afterwards chip sampled.

Coarse adjustments of the tripod for positioning the probe centrally in front of each half rectangle was rather difficult in the stope, and usually required more time than that needed for the actual counting. Fine adjustment to a precalibrated 40mm effective probe-sample distance could, however, be made within seconds.

At convenient points, where a high gold value was found by the measurements referred to above, a few extra measurements were made to explore the spatial distribution of the gold in the region in which it was concentrated.

The distance resolution for the calibrated measuring geometry used was sufficient to show that vertical distribution of gold was no more than 50mm. Abrupt changes in concentration were observed over about 20mm in the direction normal to the face. This evolved from repeat XRF measurement after chip sampling.

14.1.4 Details of the fluorescence measurements

In the tests the probe was adjusted before each measurement to give a total count rate equal to that obtained when the

probe was 40mm from a smooth rock surface. It was calculated that at this distance the sample of solid rock from which more than 90% of the measured intensity was received was equivalent to a bowl-shaped mass 10cm in diameter and 2,5cm deep.

The instrument was initially calibrated by means of powdered homogeneous samples. The calibration was later adjusted to the inhomogeneous, layered structure of the reef. It was later found that this adjustment had not been quite accurate, and that there had been some residual bias. A more precise calibration factor for a layered structure still had to be determined.

It was realized that the thickness of the gold-bearing layer influences the calibration factor to some extent. In these tests the thickness of the visible reef was consistently less than 50mm. It was estimated that any variation in thickness between 0 and 50mm could only have resulted in a shift in the calibration factor of less than about 7%.

The exposed rock face was measured at fixed positions for two counting periods of 100 seconds each. The counts analysed in each channel were displayed on the elecronic package. The gold content expressed in terms of either g/t or cm.g/t could then be calculated directly from the readings.

The random counting error amounted to an almost constant absolute standard deviation of 17g/t or 140cm.g/t gold in each pair of analyses. Because of this statistical error, negative values for the gold content were sometimes obtained

at low concentr ions (<25g/t or 200cm.g/t).

The coefficient of variation,, CV, i.e. the relative statistical error, was inversely proportional to the gold concentration; the total random error in the fluorescence sampling and analysis of individual values below 1000cm.g/t was thus predominantly the linear 140cm.g/t standard deviation resulting from counting statistics.

14.1.5 Details of chip sampling and analysis

Chip smamples at the mine had a nominal standard height of 80mm and a nominal depth of 20mm into the face. A nominal width of 150mm was chipped in the tests to permit comparison with flourescence measurements made at two adjacent points.

At the test site it was difficult to cut samples of the required size because of the transition from quartzite in the hangingwall to shale in the footwall. The chipping depth of individual samples was observed to vary from 5mm to 60mm over the height of the sample, while the mean height varied from 60 to 100mm and the mean width from 120 to 220mm. In other words the ratio of sample mass to projected area of the gold-bearing part of the sample varied significantly, which does affect the evaluation when sampling a thin layered deposit. It would be extremely difficult to overcome variations of this kind in this particulaar area and the precision of the results obtained would be significantly affected for this reason.

The time taken to chip a sample was approximately the same as the actual counting time (excluding set-up time) in the fluorescence measurement of the same sample. The chip samples were taken to the assaying department where they

were individually crushed, ground to -150µm and well mixed. Duplicate fire assays for gold on weighed portions of the homogeneous sample agreed to within about 10cm.g/t.

14.1.6 Comparison of XRF and chip sample values

In Figure 14.1 fire assay values of several contiguous groups of individual chip samples are plotted; directly above these the corresponding fluorescence values are shown. It will be observed that there is, generally, good correlation between the upper and lower patterns. The means of sample groups are given in Table 14.1, and the correlation coefficients between XRF and chip values in Table 14.3, and the probability that the coefficients could have resulted from purely random fluctuation is evaluated using a transformation due to R.A.Fisher (Davies 1950). Group means and their standard deviations are shown in Figure 14.2.

Table 14.1 Comparison of means of XRF and chip samples

Sample group	XRF Mean	Chip Mean	N
A	9,7	10,4	11
B	56	56	19
C	77	93	10
D	38	38	23
E	57	69	27
F	120	103	19
G	45	17,7	29
H	38	32	16
A to H	62,9 (σ=60)*	57,7 (σ=72,7)	136
A to F and H**	67,9 (σ=64,9)	68,3 (σ=77,6)	107

* σ = standard deviation of mean

** Group G eliminated because the results were suspect

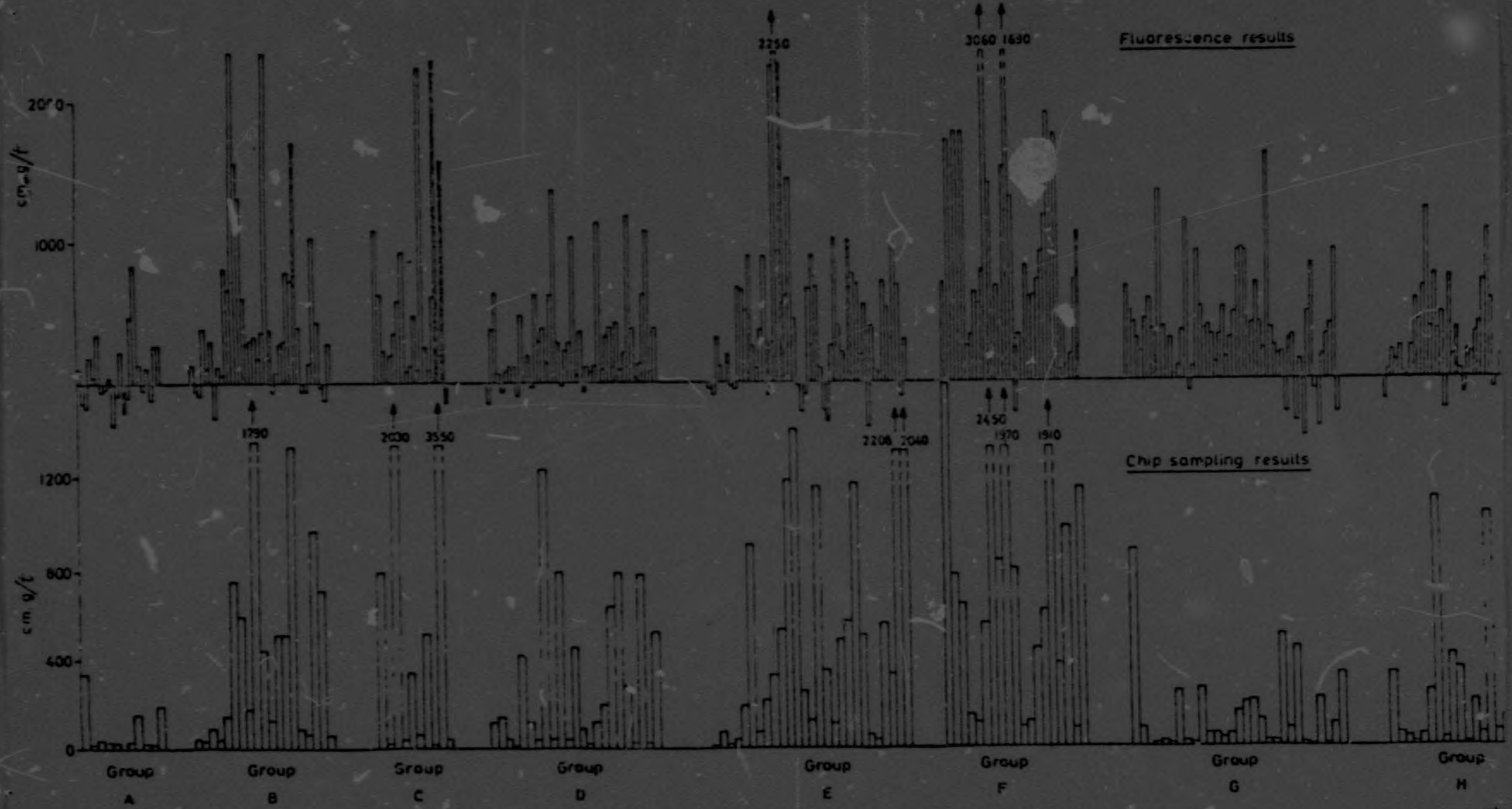


FIGURE 14.1 FLUORESCENCE AND CORRESPONDING CHIP SAMPLE VALUES FROM LESLIE GOLD MINE

Table 14.2 Correlation between XRF and chip values

Comparison	N	r	Fisher transf. $z=0,5\ell n(\frac{1+r}{1-r})$	$1/\sqrt{(N-3)}$	Null Probability
Individual samples	136	0,442	0,47	0,086	10^{-6}
Groups A to H	8	0,911	1,35	0,44	0,002
Groups A - F and H*	7	0,95	1,83	0,5	0,001

* Group G eliminated because results were suspect

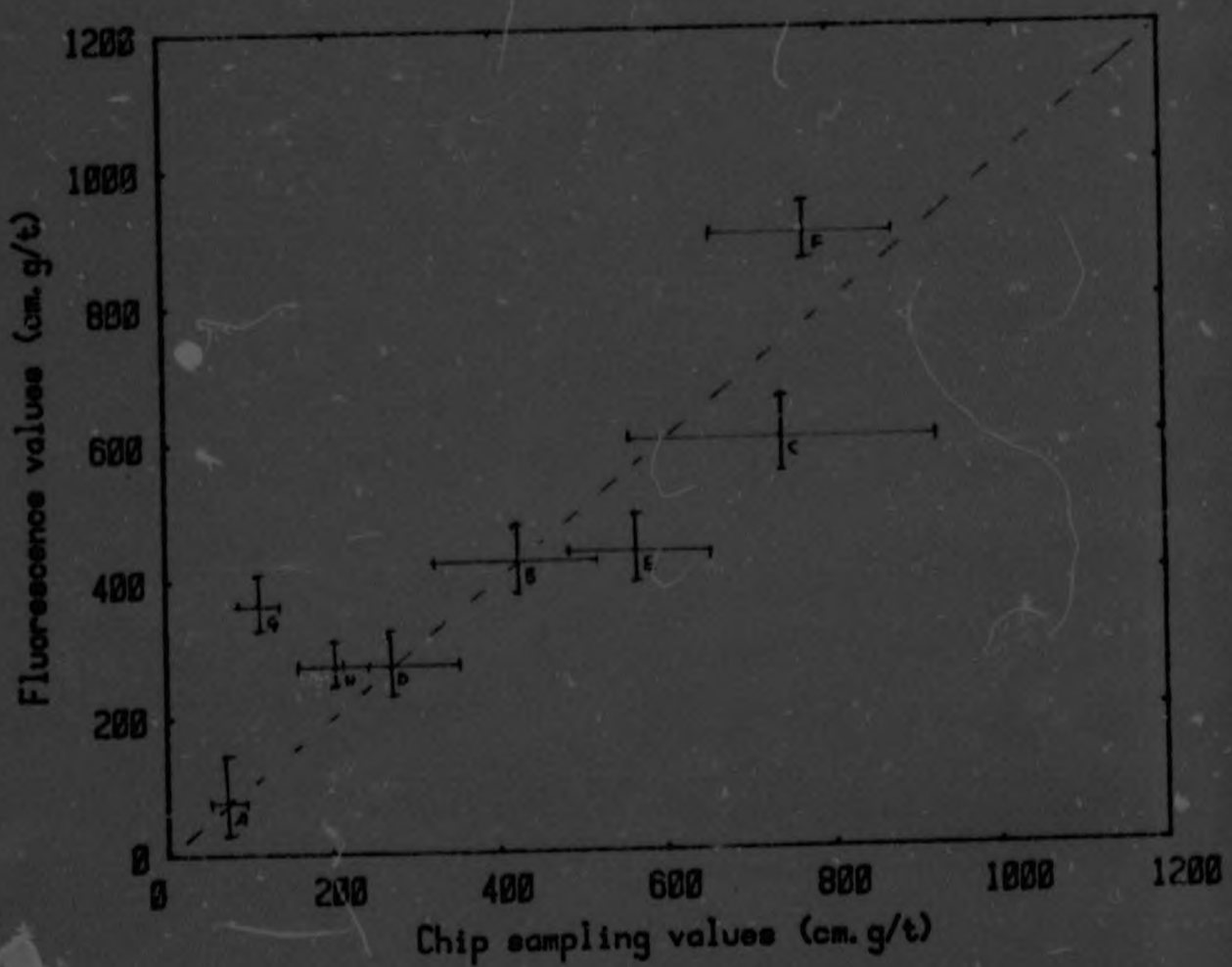


Fig. 14.2 Group means of fluorescence and chip values

This statistical analysis shows that the means of the results obtained from chip sampling and assaying agree very well with those obtained by the flourescence method. This holds true for corresponding results obtained from individual measurements as well as those from groups of contiguous samples.

Once the close linear relationship between the XRF and the chip values had been shown, estimates of the variation in the underlying gold distribution and of the variation in the chip sampling method could be made, since the variation in the XRF method was reasonably well known and small because of the large number of repeat measurements done.

The coefficient of variation, i.e. relative standard deviation of measured values is made up of the coefficient of variation of measuring, CV_m, and that of the underlying gold distribution, CV_g, summed in quadrature:

$$CV^2 = CV_m^2 + CV_g^2$$

The XRF measurements have a $CV^2 = (60/62,9)^2 = 0,91$ (excluding group G, $CV^2 = (64,9/67,9)^2 = 0,91$). The standard deviation of the XRF measurements, known from Poisson statistics, is approximately 17g/t, which gives $CV_m^2 = (17/62,9)^2 = 0,07$ (= 0,06 excluding group G).

Thus $CV_g = \sqrt{0,84} = 0,92$ (=0,92 excluding group G). It can be reasonably assumed that for over 100 corresponding measurements the underlying CV_g must have been very similar for both the fluorescence and chip values. The measured chip values have $CV^2 = (72,7/57,7)^2 = 1,59$ (=1,28 excluding group G); subtracting the CV_g^2 found above leaves for the chip sampling plus assaying $CV_m = \sqrt{0,75} = 0,87$ (=0,66 excluding

group G).

The derivation of the value of the CV_m for chip sampling and assaying is insensitive to errors in the estimation of the CV_m of the fluorescence measurement. It does, however, rely on the assumption of a similar value for CV_g which becomes less accurate when fewer than about 100 samples are compared.

These calculations show that the variation in the fluorescence method in these tests was much less than the variation in the chip sampling method for equal chipping and measuring times.

The above comparison may also be interpreted as indicating that for a specific measuring precision the fluorescence measurement was approximately ten times faster than the taking of chip samples.

14.1.7 Discussion

The results from the site at Leslie Gold Mines Ltd. had shown that at that site it was feasible to perform the *in situ* determination of gold on a stope face by means of a gamma-ray fluorescence analyser. It was also found that, whereas a continuous sample along the face yields the true average value of the face, samples taken over short distances every few metres may not give a true reflection of the value.

Whether the feasibility could be demonstrated at any other site was not certain. It was thought that in going to wider reefs or rock with better chipping characteristics the chip sampling precision could possibly improve to a greater extent than the precision in the XRF measurements. The

observed ten-fold speed advantage of the XRF measurement, when adjusting the measurement time to obtain the same precision as in chip sampling, would the be somewhat diminished but even for very wide reefs of much lower local concentration it was thought that there should still remain some advantage.

While it had been shown at Leslie that the fluorescence method of measurement was feasible, it had not yet been shown that it was practical.

In the tests the overall measuring speed, including positioning of the probe, was far slower than the actual measuring speed. To make the method practical and thus attain the abovementioned speed advantage over chip sampling, a far lighter and more robust instrument than was used in these tests had to be developed. It was realised that the electronic package needed to be easily portable but the probe, in particular, had to be convenient for continuous, rapid hand scanning of the face. At that stage the development entailed largely an adaption and integration of technology then available and did not appear to present any fundamental difficulties.

The equipment used in these tests was for various reasons operated considerably below its maximum measuring speed. The experience gained in these tests led to several simple modifications in the design of subsequent instruments which resulted in about an order of magnitude in increase in measuring speed.

At that stage little was known as to what the optimum measuring speed should be. It was realized, however, that

Author Rolle R
Name of thesis Gamma Ray Fluorescence for In Situ evaluation of ore in Witwatersrand Gold Mines 1979

PUBLISHER:
University of the Witwatersrand, Johannesburg
©2013

LEGAL NOTICES:

Copyright Notice: All materials on the University of the Witwatersrand, Johannesburg Library website are protected by South African copyright law and may not be distributed, transmitted, displayed, or otherwise published in any format, without the prior written permission of the copyright owner.

Disclaimer and Terms of Use: Provided that you maintain all copyright and other notices contained therein, you may download material (one machine readable copy and one print copy per page) for your personal and/or educational non-commercial use only.

The University of the Witwatersrand, Johannesburg, is not responsible for any errors or omissions and excludes any and all liability for any errors in or omissions from the information on the Library website.